Scilight

Sustainable Engineering Novit
https://www.sciltp.com/journals/sen

Review

Hybrid and Flow-Electrode Capacitive Deionization: Materials Design, Multispecies Removal, and Smart Regulation

Yuan Gao, Chengan Ye, Rui Wang, Wenting Li * and Huan Pang *

School of Chemistry and Materials, Yangzhou University, Yangzhou 225002, China
* Correspondence: wtlichem@yzu.edu.cn (W.L.); panghuan@yzu.edu.cn or huanpangchem@hotmail.com (H.P.)

How To Cite: Gao, Y.; Ye, C.; Wang, R.; et al. Hybrid and Flow-Electrode Capacitive Deionization: Materials Design, Multispecies Removal, and Smart Regulation. *Sustainable Engineering Novit* **2025**, *1*(1), 7. https://doi.org/10.53941/sen.2025.100007

Received: 22 September 2025
Revised: 14 November 2025
Accepted: 4 December 2025
Published: 23 December 2025

Abstract: As an emerging desalination technology, capacitive deionization (CDI) has garnered significant attention due to its superior energy efficiency and performance metrics compared to conventional distillation and reverse osmosis (RO) techniques. Over the past decade, substantial advances have been achieved across multiple technical dimensions of CDI systems. This review focuses on two representative CDI architectures-hybrid capacitive deionization (HCDI) and flow-electrode capacitive deionization (FCDI)-highlighting their core innovation mechanisms: the ion storage behavior in HCDI and the continuous operation characteristics of flow electrodes in FCDI. We systematically examine recent research progress in critical areas including innovative electrode materials, optimized cell configurations, and expanded contaminant removal targets (e.g., heavy metals/organic pollutants), while delving into machine learning (ML)-driven strategies for operational parameter optimization and system performance prediction. Ultimately, by synthesizing these technological breakthroughs and aligning them with current engineering requirements, this review aims to facilitate the scalable implementation and industrial adoption of CDI technology within sustainable water treatment frameworks.

Keywords: capacitive deionization; electrode materials; cell design; ion removal; modeling

1. Introduction

Water, as an indispensable fundamental resource on Earth, sustains biological existence, drives economic development across industries, and permeates all facets of daily life [1,2]. Although approximately 71% of the planet's surface is covered by water, 97.5% constitutes saline water unsuitable for direct utilization, with merely 2.5% classified as freshwater [3]. Consequently, over one-quarter of the global population faces extreme water scarcity, a crisis severely threatening sustainable human development and essential ecosystem functions [4–6]. To address escalating potable water demands and water shortage challenges, desalination technologies have spurred extensive worldwide research [7–12]. Conventional desalination techniques consume electrical, thermal, or mechanical energy to remove salts from seawater/brackish water, producing freshwater that meets municipal, industrial, and agricultural requirements. Current technology paradigms are dominated by thermal processes (e.g., multi-stage flash, MSF [13]) and pressure-driven membrane processes (e.g., reverse osmosis, RO [14–16]), collectively accounting for 87% of global desalination capacity. Alternative approaches such as nanofiltration (NF) [17–20], forward osmosis (FO), and electrodialysis (ED) [21,22] still exhibit significant energy consumption bottlenecks. In contrast, capacitive deionization (CDI) technology leverages electrosorption and redox reactions at electrode interfaces to achieve ion removal, offering integrated advantages of low energy consumption, high ion selectivity, and

environmental compatibility [23–26]. Figure 1 shows the advantages of the CDI system for salt ion adsorption/desorption.

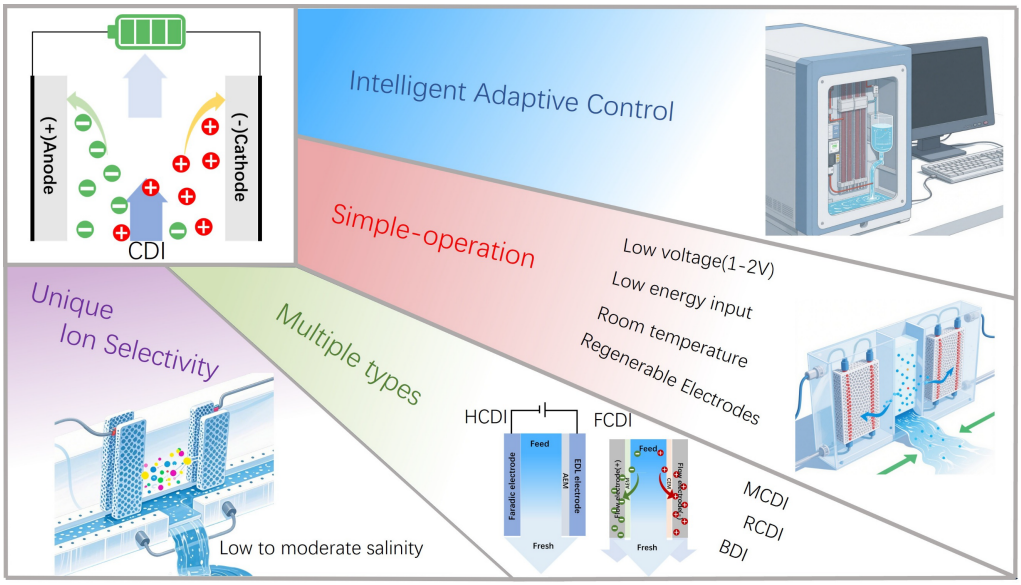

Figure 1. Summary of various CDI advantages.

The first generation of CDI systems emerged in 1960, featuring a fundamental configuration consisting solely of electrode assemblies and a direct current power source. Subsequent technological advancements led to the development of membrane capacitive deionization (MCDI) by integrating ion-exchange membranes (IEMs) at the electrode-water flow channel interface [27–29]. Building upon this architectural innovation, the use of flowing carbon slurry electrodes instead of static electrodes successfully established the flow-electrode capacitive deionization (FCDI) system [30–32]. In this setup, peristaltic pumps continuously deliver the slurry into electrode chambers, enabling continuous desalination of high-concentration solutions. Further iterations introduced pseudocapacitive electrodes into the CDI framework, giving rise to hybrid capacitive deionization (HCDI) technology [33–35]. Its core mechanism relies on rapid faradaic redox reactions occurring at or near the electrode surface for ion removal. Notably, the incorporation of faradaic materials creates a pseudocapacitive storage mechanism based on redox reactions, forming a dual synergistic hybrid energy storage behavior that effectively overcomes the capacity limitations of traditional electric double-layer (EDL) capacitor materials. This breakthrough has spurred the emergence of advanced systems such as rocking-chair capacitive deionization (RCDI) [36–38] and battery deionization (BDI) [39–41].

This review focuses on the technological advancements in HCDI and FCDI, excluding other configurations such as MCDI and RCDI. This selectivity stems from the unique design philosophies of these two systems and their transformative impact on the CDI field. First, electrode materials serve as the core element of CDI systems, directly determining desalination performance. By replacing traditional porous carbon electrodes with faradaic materials, HCDI significantly enhances device desalination efficiency. Recent research has achieved breakthroughs in the development of novel faradaic materials, with representative examples including transition metal sulfides (TMS) [42], MXenes [43–45] and prussian blue analogues (PBAs) [46–48], among which cathode intercalation materials have also been extensively explored. The HCDI system integrates the redox reactions of "battery-type" electrodes with the EDL adsorption mechanism, creating a synergistic desalination effect characterized by high capacity and efficiency. Through material optimization strategies such as core-shell structure design and heterointerface engineering, HCDI electrodes demonstrate significantly improved structural stability during long-term charge-discharge cycles. FCDI represents a significant innovation within the CDI technology field. Unlike conventional CDI systems that employ fixed solid-state electrodes, the effective capacity of electrodes in FCDI units is dynamically adjustable, and its desalination capability is no longer constrained by the inherent capacity of fixed electrodes. This unique advantage endows FCDI with significantly enhanced salt removal capacity, making it particularly suitable for treating high-salinity water sources (such as seawater). Furthermore, FCDI systems can operate continuously without requiring discharge regeneration steps. Common electrode materials for FCDI include activated carbon (AC) and its derivatives, while novel materials such as hydrogels and metal-organic frameworks (MOFs) have also been explored. Notably, efficient electron and ion transport is a critical factor determining the desalination efficiency of FCDI systems [49]. Moderate mass loading

facilitates contact between AC particles or between particles and the current collector, thereby enhancing electron conduction; however, excessive mass loading may increase the risk of clogging and elevate pumping energy consumption [50]. Consequently, substantial research focuses on exploring superior electrode materials and their optimal loading levels, often through the incorporation of redox-active species to improve electron transfer and enhance system performance. Recently, a novel design utilizing magnetic fields to precisely regulate the motion of the flow electrode (slurry) has been developed, offering the potential for more precise operational control of FCDI systems. In the future, such enhancements in control precision will significantly expand the application potential of FCDI. Beyond the aforementioned core components, optimizing the design of current collectors and the overall FCDI system configuration also constitutes a major research priority.

HCDI and FCDI represent two advanced derivatives of conventional CDI, each exhibiting distinct performance characteristics rooted in their fundamental operational mechanisms. A direct comparison across key metrics reveals their complementary strengths and limitations. In terms of salt adsorption capacity, HCDI often demonstrates high values per batch (30–80 $mg \cdot g^{-1}$) by leveraging Faradaic battery-grade materials [51–54], whereas FCDI achieves theoretically unlimited and continuous desalination through circulating flow electrodes, offering superior total treatment capability [55]. Regarding energy consumption, HCDI generally operates more efficiently, particularly in brackish water, due to its lower operating voltage and absence of pumping systems; in contrast, FCDI incurs significant auxiliary energy expenditure for slurry circulation [56–58]. Cycle stability presents a major differentiator: HCDI performance degrades over hundreds to thousands of cycles due to structural fatigue of the intercalation electrodes [59–61], while FCDI exhibits exceptional long-term stability as the flow electrode is continuously regenerated externally. Concerning applicability across salinities, HCDI is optimal for low-salinity brackish water desalination [62], whereas FCDI's adaptable operation makes it highly effective across a broader range, including seawater and industrial brine concentration [63,64]. Finally, their operational modes are inherently different-HCDI functions in a batch-wise manner requiring periodic electrode regeneration, while FCDI enables true continuous processing, a critical advantage for scaling and integration into industrial water treatment trains.

This review systematically evaluates the technical characteristics of HCDI and FCDI from the perspective of electrode materials and device configurations. It specifically elucidates novel electrode materials, structural innovations, and their application potential. Building upon recent advancements in CDI technology, the work further proposes that continuous refinement of electrode-device synergistic mechanisms and their deep integration with modern technologies are essential to expand the application prospects of this technology.

2. Hybrid Capacitive Deionization

CDI systems store ions via the EDL mechanism, with their adsorption capacity constrained by the electrode's specific surface area (SSA) (typically < 20 $mg \cdot g^{-1}$ for AC electrodes [65]). In contrast, HCDI technology employs faradaic-active electrode materials (e.g., metal oxides, conductive polymers, and sodium-ion battery materials). By coupling EDL storage with faradaic redox reactions, HCDI establishes multiple ion adsorption pathways to enhance system efficiency. Consider a representative HCDI configuration: The system replaces conventional carbon electrodes with a $Na_4Mn_9O_{18}$ (NMO) electrode, combined with an anion-exchange membrane (AEM) and a porous carbon electrode in a layered assembly. During desalination, sodium ions are stored via intercalation reactions in the NMO electrode, while chloride ions are adsorbed within the EDL formed at the porous carbon electrode surface. The NMO electrode requires no additional ion-selective membrane due to the manganese oxide's intrinsic cation selectivity. However, to prevent desalination efficiency decay caused by cation adsorption on the carbon electrode, an AEM is positioned adjacent to the carbon electrode to block cation permeation. Testing demonstrates that this system achieves a desalination capacity of 31.2 $mg \cdot g^{-1}$ across broad NaCl concentration ranges [52]. By synergizing EDL adsorption and faradaic reaction mechanisms, HCDI technology significantly enhances desalination efficiency, energy recovery capability, and multi-scenario applicability, representing a significant advancement toward next-generation high-efficiency water treatment technologies.

2.1. HCDI Cathode

HCDI technology faces two key challenges: (i) Inter-electrode kinetic mismatch-the rate disparity between rapid EDL adsorption on carbon electrodes and diffusion-controlled faradaic reaction kinetics constrains desalination efficiency; (ii) Structural degradation of faradaic materials during ion storage, compromising long-term system stability. To address these limitations, recent research focuses on developing novel electrode material systems including TMS, MXenes, PBAs, layered double hydroxides, and conductive polymers. Concurrently,

systematic optimization of electrode microarchitecture design synergistically enhances reaction kinetics and cycling stability.

2.1.1. TMS

TMS feature a characteristic sandwich-like S-Mo-S layered structure. Their large interlayer spacing-particularly exemplified by MoS_2-provides abundant ion storage sites and rapid intercalation kinetics when utilized as sodium-ion capturing electrodes in HCDI systems, effectively addressing key limitations of conventional HCDI. Under an applied electric field, MoS_2 undergoes reversible redox reactions, driving valence transitions ($Mo^{4+} \leftrightarrow Mo^{5+}/Mo^{3+}$) accompanied by electron transfer. This process achieves charge compensation through adsorption of counterions from the electrolyte, thereby significantly enhancing desalination performance. However, the 2D MoS_2 structure exhibits a pronounced tendency for interlayer aggregation, resulting in substantially constrained cycling durability in MoS_2-based HCDI systems. Pan et al. [66] constructed a MoS_2/MXene heterostructure by compositing MoS_2 with MXene. As revealed by the scanning electron microscopy (SEM) images in Figure 2a,b, marked structural differences are evident: pure MoS_2 exhibits an irregular, wrinkled morphology, whereas the MoS_2/MXene heterostructure displays an ordered layered structure with enhanced interfacial contact. This design utilizes two-dimensional MXene and MoS_2 to construct a three-dimensional "mutually supporting" framework, effectively suppressing structural agglomeration. Simultaneously, the MXene component significantly enhances the conductivity of the system, thereby synergistically improving its desalination capacity and rate. Experimental results demonstrate that the heterostructure achieves a desalination capacity of 23.98 mg g^{-1} and a desalination rate of 4.6 mg $g^{-1}\cdot min^{-1}$, with only 4% capacity decay after 100 cycles. Inspired by research on MoS_2, Tang et al. [67] noted that $MoSe_2$ possesses a similar Se-Mo-Se sandwich structure, yet exhibits higher electrical conductivity and larger interlayer spacing than MoS_2. They pioneered the application of $MoSe_2$ in a HCDI system via a solvothermal method, successfully fabricating a $MoSe_2$/MCHS composite material (structural model shown in Figure 2c). The MCHS framework not only effectively stabilizes $MoSe_2$ but also endows the composite with excellent hydrophilicity, high electrical conductivity, low ionic resistance, and a rich mesoporous structure. These characteristics synergistically facilitate rapid ion transport and prevent structural agglomeration. When treating a 500 mg·L^{-1} NaCl solution under an applied voltage of 1.2 V, the composite material achieves an adsorption capacity of 45.25 mg·g^{-1} and an adsorption rate of 7.75 mg·$g^{-1}\cdot min^{-1}$. Furthermore, the composite exhibits significantly enhanced capacity retention after multiple charge-discharge cycles.

TMS exhibit superior performance to oxides in terms of ion storage kinetics, capacity, and cycle life, owing to their large interlayer spacing, high conductivity, and multi-electron redox properties. These advantages make them particularly suitable for high-power-density desalination systems and next-generation energy storage devices. However, the inherent thermodynamic metastability of TMS materials poses a challenge to their practical application, necessitating multiscale structural design and interface engineering to reconcile the stability-performance trade-off. Furthermore, machine learning (ML)-integrated high-throughput screening can effectively accelerate the discovery of stable sulfide materials.

2.1.2. MXenes

MXenes, a class of two-dimensional transition metal carbides and nitrides featuring inherent hydrophilicity and metallic conductivity, have demonstrated tremendous promise for high-rate pseudocapacitive energy storage applications. Usually, MXenes are synthesized from ternary layered ceramic materials such as MAX phases ($M_{n+1}AX_n$, where M is an early transition metal, A is an element from groups 13–16, X is carbon and/or nitrogen, and n = 1–4). MXene synthesis involves selective etching of the A group element from its parent MAX phase, following an intercalation-assisted delamination. The resulting MXene can be represented by the general formula $M_{n+1}AX_n$, where T_x denotes the termination groups (-F, -Cl, -O, and -OH), which are responsible for the hydrophilicity of MXenes. MXenes have demonstrated a unique combination of 2D morphology and the ability to intercalate various cations spontaneously with subsequent surface redox reactions.

Gogotsi et al. [68] first reported the application of MXene materials in HCDI technology. They designed a dual-stacked electrode architecture based on size-graded $Ti_3C_2T_x$ MXene nanosheets, with experimental validation confirming its significant potential for HCDI. This work laid a crucial foundation for subsequent MXene-based desalination research. However, follow-up studies revealed that pristine MXene tends to undergo aggregation and restacking, leading to diminished cycling stability. The introduction of functional interlayer mediators between MXene sheets has proven effective in enhancing electrochemical performance and structural integrity, driving continuous modification efforts. Wang's team employed conductive polypyrrole (PPy) as an intercalating agent. The incorporation of PPy not only expanded the MXene interlayer spacing to 1.57 nm (effectively suppressing

self-restacking) but also formed an antioxidative protective layer. Electrochemical tests demonstrated that the $Ti_3C_2T_x$ @PPy composite exhibits high specific capacitance (345.8 $F \cdot g^{-1}$) and low charge transfer resistance. It delivered excellent desalination performance in 100 $mg \cdot L^{-1}$ NaCl solution while maintaining high efficiency even in the presence of heavy metal ions [69]. Jin et al. [70] utilized a molten salt etching strategy to grow NiCo prussian blue (PB) nanocubes in situ on Ni-doped $Ti_3C_2T_x$ nanosheets, constructing a $Ti_3C_2T_x$/Ni/NiCo-PBA composite electrode (Figure 2d). The NiCo-PBA nanocubes effectively inhibited MXene restacking, increased lattice spacing, and facilitated salt-ion diffusion/storage, achieving a desalination capacity of 53.22 $mg \cdot g^{-1}$. Notably, the material demonstrated remarkable cycling stability—after 20 cycles, the capacity fluctuated minimally from 56.8 to 57.0 $mg \cdot g^{-1}$.

Although these interlayer modification strategies enhance adsorption performance and stability, their complex fabrication processes and high costs impede scalable application. Consequently, developing low-cost, readily available, and easily synthesized alternatives has become a research priority. Mahmoud's group developed a chitosan-lignosulfonate/MXene (CLM) nanocomposite using chitosan-lignosulfonate nanospheres (CSLS) as interlayer mediators. The CSLS integration expanded the MXene interlayer spacing from 1.32 nm to 1.57 nm, effectively suppressing stacking while leveraging the inherent cost-effectiveness and eco-friendliness of chitosan and lignosulfonate as natural biopolymers [71].

The stability of MXenes in CDI applications is pivotal for their practical deployment, a property fundamentally governed by their synthesis and post-processing conditions. Primarily, the choice of synthesis route-such as HF etching, in situ HF formation, or Lewis acid molten salt etching-directly predetermines the material's surface terminal chemistry (e.g., the ratio of -F, -O, and -OH groups). This not only dictates the initial hydrophilicity and electrical conductivity but also lays the foundation for its anti-oxidation stability in aqueous environments [72]. Building upon the synthesis, molecular-level interfacial engineering for precise modulation of surface chemistry has proven to be an effective strategy for enhancing stability. For instance, the construction of an interfacial hydrogen-bond network using phytic acid (PA) can effectively activate and stabilize the reactive -OH terminals, thereby significantly boosting oxidation resistance while simultaneously enhancing capacity [73]. Furthermore, the selection of transition metal elements constitutes another critical dimension for tuning the intrinsic stability of MXenes. Vanadium (V)-based MXenes, for example, demonstrate superior structural stability and electron transport capability compared to conventional titanium (Ti)-based MXenes, attributed to their multivalent d-orbital electron configuration and abundant defects, offering a new material choice for designing long-lasting CDI electrodes [74]. MXenes hold great promise for HCDI, owing to their high electrical conductivity that ensures fast charge-transfer kinetics and a tunable interlayer spacing that enables high ion storage capacity. Their practical deployment, however, is challenged by two main factors: an inherent susceptibility to surface oxidation, which compromises long-term stability and requires mitigation via surface engineering or protective layers, and synthesis procedures that involve corrosive reagents, raising safety and environmental issues [75–77]. A thorough evaluation is therefore essential to navigate the trade-offs between their performance benefits and the imperatives of cost, durability, and safe operation.

2.1.3. PBAs

The chemical formula of PB is $Fe_4[Fe(CN)_6]_3 \cdot xH_2O$, featuring a three-dimensional cubic lattice structure formed by low-spin Fe^{2+} and high-spin Fe^{3+} bridged via cyanide ligands (CN^-). This open framework contains nanoscale pores (approximately 4.6 Å in diameter), enabling reversible insertion/extraction of water molecules or ions (e.g., Na^+, K^+). Owing to its high theoretical capacity, open framework structure, and tunable active sites, this material has attracted considerable attention [46,78–80].

However, studies reveal that PBAs with single active sites, such as NiFe PBAs and ZnFe PBAs, often exhibit low sodium storage capacity due to structural defects and hindered ion diffusion. In contrast, dual-active-site PBAs (e.g., CoFe PBAs) demonstrate higher theoretical capacities through synergistic interactions between metals. Consequently, PBAs with dual or multi-metal active sites are more suitable for CDI electrodes. To this end, Wang et al. [81]. synthesized a dual-active-site PBA using a two-step co-precipitation method (Figure 2e). By adjusting the concentration of the shell-growth precursor, they encapsulated high-capacity CoFe PBA within a robust NiFe PBA shell, successfully fabricating a core-shell heterostructure (CoFe@NiFe PBA) with optimized shell thickness. This strategy leverages the exceptional stability of NiFe PBA to encapsulate dissolution-prone CoFe PBA, preserving the high theoretical capacity of CoFe PBA while mitigating common PB issues such as dissolution sensitivity and volume expansion. The heterostructured PBA with optimal shell thickness achieved a high desalination capacity of 49 $mg \cdot g^{-1}$ in 4000 $mg \cdot L^{-1}$ saline solution, maintaining 92.6% capacity retention after 50 cycles and 77.7% after 200 cycles-significantly outperforming single-active-site PBAs.

To further address the low conductivity and structural collapse of PBAs, Wang et al. [82] constructed a CoNi-PBA@Co/N-HC heterostructure by anchoring cobalt-doped nickel hexacyanoferrate (CoNi-PBA) onto ZIF-67-derived Co/N co-doped hollow porous carbon (Co/N-HC). The confinement effect of Co/N-HC effectively suppresses structural collapse in PBAs, substantially improving the poor cycling stability of conventional PBAs. Additionally, this material maintains efficient desalination performance across a wide salinity range.

Recently, Ding et al. [83]. reported a novel strategy: combining glycerol ligands with metal ions (Mn^{2+}, Co^{2+}) to form uniform metal-glycerate solid spheres via solvothermal reaction, followed by introducing potassium ferrocyanide solution to synthesize ternary-metal CoMnFe-PBA. The hollow sphere structure (CoMnFe-PBA-HS) prepared through this process effectively mitigates severe lattice distortion during charge/discharge cycles induced by trimetallic incorporation. Subsequently, CoMnFe-PBA-HS was composited with MXene via electrostatic self-assembly (Figure 2f). In this composite, CoMnFe-PBA alleviates lattice distortion during cycling, while MXene provides structural support to prevent PBA collapse. Their synergistic interaction constructs 3D ion channels that facilitate rapid Na^+ diffusion and storage. When applied in HCDI systems, the material exhibits an adsorption capacity of 185.25 $mg \cdot g^{-1}$ at 1.4 V and 20 $mA \cdot g^{-1}$, with no observable capacity decay after 80 cycles.

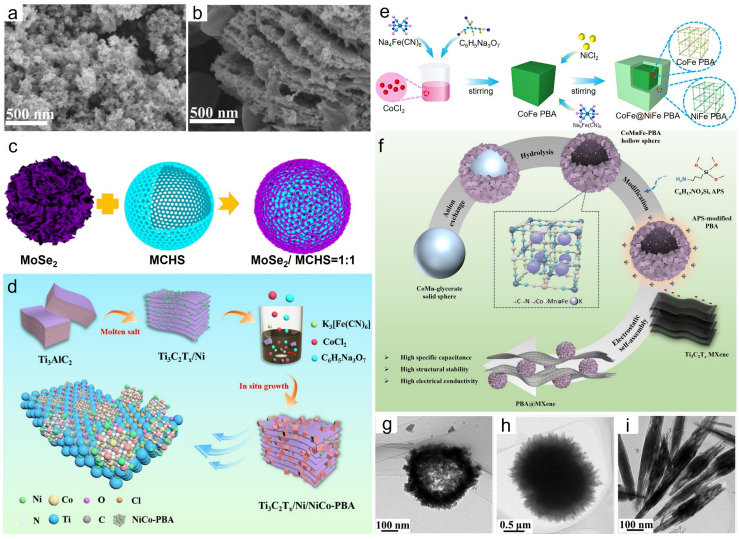

Figure 2. SEM images of MoS_2 (**a**) and MoS_2/MXene heterostructure (**b**). Reprinted with permission from Ref. [66]. Copyright 2022, Elsevier. (**c**) Schematic diagram of the $MoSe_2$/MCHS composite with a 1:1 $MoSe_2$-to-MCHS ratio. Adapted with permission from Ref. [67]. Copyright 2023, Elsevier. (**d**) The synthesis process of $Ti_3C_2T_x$/Ni/NiCo-PBA composites. Reprinted with permission from Ref. [70]. Copyright 2024, Elsevier. (**e**) Schematic illustration of the preparation procedure of CoFe@NiFe PBA. Reprinted with permission from Ref. [81]. Copyright 2024, Elsevier. (**f**) Schematic illustration of the preparation process of PBA@MXene. Reprinted with permission from Ref. [83]. Copyright 2025, Elsevier. TEM images of HWC (**g**), UWC (**h**) and NWC (**i**). Reprinted with permission from Ref. [84]. Copyright 2023, Elsevier.

In summary, multi-active-site PBAs demonstrate superior synergistic desalination performance in HCDI applications. Through crystal structure modulation or defect engineering, high-density active sites can be introduced while preserving the intrinsic 3D ion channels of PBAs, significantly increasing surface adsorption sites and faradaic reaction sites. During desalination, these sites concurrently capture multiple ions via EDL capacitance and redox reactions. This enhanced charge storage mechanism overcomes the performance limitations of conventional single-site materials, maintaining high desalination efficiency even at elevated salt concentrations while exhibiting superior cycling stability compared to traditional PBAs. Nevertheless, excessive increases in active site density may cause structural disorder, necessitating a balance between site density and crystal integrity to ensure long-term cycling durability. Furthermore, combining PBAs with highly conductive carriers or applying surface modifications can further optimize electron transfer efficiency, offering new pathways for developing high-performance HCDI electrodes.

2.1.4. Other

The asymmetric structure of HCDI systems often leads to ion storage imbalance, thereby constraining their desalination performance. Zhang et al. [85]. proposed optimizing HCDI systems by modulating the electrode mass ratio. Their study demonstrated that a system employing $NaTi_2(PO_4)_3$/reduced graphene oxide composite (NTP-

rGO-700) as the cathode and AC as the anode achieved optimal performance when the cathode-to-anode mass ratio was 2:1. Furthermore, the structural characteristics of electrode materials significantly influence their performance [86]. Tang et al. [84] recently evaluated three configurations of carbon-encapsulated $W_{18}O_{49}$: nanowires (NW), urchin-like nanowires (UW), and hollow nanowires (HW) (Figure 2g–i). Among these, the urchin-like $W_{18}O_{49}$@C (UWC) exhibited the most superior comprehensive performance, including the optimal pore size distribution, the largest SSA and specific capacitance, and the highest graphitization degree and carbon content. Under batch-mode operation at 1.2 V with an initial NaCl concentration of 1000 $mg \cdot L^{-1}$, the UWC electrode achieved a salt adsorption capacity (SAC) of 32.25 ± 0.70 $mg \cdot g^{-1}$. This electrode also demonstrated robust cycling stability, high charge efficiency (CE), and low energy consumption. These results underscore the importance of increasing pore size and SSA for enhancing the efficiency of CDI systems. Collectively, the aforementioned studies not only deepen the understanding of the structure-performance relationship in electrode materials but also establish a solid foundation for developing novel, high-performance, and low-cost CDI electrode materials.

2.2. HCDI Anode

Currently, research on cathode materials receives extensive attention, while studies on anode materials remain relatively scarce. Existing primary materials for anion removal, such as Ag/AgCl and Bi/BiOCl, suffer from sluggish dechlorination kinetics and susceptibility to hydroxide precipitation. Furthermore, silver-based electrodes are prohibitively costly [87–89]. Consequently, developing efficient, stable, reversible, and low-cost chloride ion storage electrodes represents a highly promising research direction. Li et al. [90] proposed a novel chloride ion-intercalation anode-ZnCo-Cl layered double hydroxide (LDH)-to enhance HCDI system performance. Upon applying a positive voltage during desalination, Zn^{2+} rapidly deintercalates from the ZnCo-Cl LDH, creating numerous Zn^{2+} vacancies. Concurrently, Cl^- ions are extracted from the solution to occupy these vacancies, while additional Cl^- ions intercalate into the LDH interlayers. When a reverse voltage is applied, Cl^- deintercalates from the LDH and releases back into the solution, simultaneously with Zn^{2+} reintercalation, ensuring the structural reversibility of the material (as shown in Figure 3a,b). Experimental results demonstrate that this electrode achieves a SAC of 56.1 $mg \cdot g^{-1}$ at 1.2 V, with an 86% capacity retention after 20 cycles. Additionally, He et al. [91] successfully fabricated a binder-free Bi@MXene film by introducing size-controlled bismuth nanoparticles into MXene nanosheets via electrostatic self-assembly. This porous film structure not only provides efficient ion diffusion pathways but also enhances the material's ion storage capacity through its three-dimensional configuration, while effectively suppressing volume expansion caused by phase transitions during conversion reactions. The HCDI cell employing the Bi@MXene film exhibits excellent desalination performance, with a SAC as high as 113.4 $mg \cdot g^{-1}$, highlighting its potential as a high-performance HCDI electrode. In summary, further exploration into anion-intercalation materials is still required, and developing suitable faradaic anode materials represents an effective strategy to address kinetic asymmetry constraints in HCDI systems.

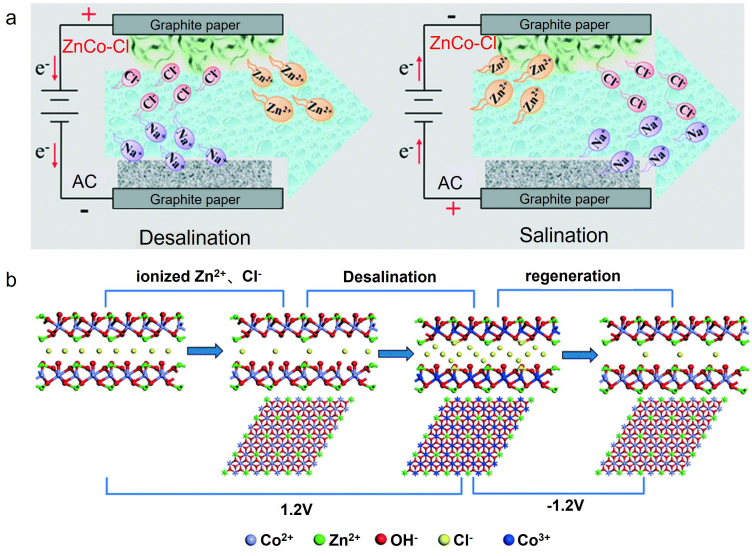

Figure 3. (**a**) The working mechanism, (**b**) the schematic of the ZnCo–Cl LDH//AC HCDI system. Reprinted with permission from Ref. [90]. Copyright 2021, The Royal Society of Chemistry.

3. Flow-Electrode Capacitive Deionization

A typical laboratory-scale FCDI system is illustrated in Figure 4a. Its core components include flow electrodes, current collectors, IEMs, and fluid channels. These components are assembled using spacers to form the fundamental FCDI unit. Feed water flows through the feed chamber located between the two IEMs. The electrode chambers are formed by the current collectors and spacers incorporating channels that guide electrode flow. Flow electrodes are continuously pumped into these chambers for circulation. During system operation, charged particles within the flow electrodes adsorb ions migrating through the IEMs. Subsequently, the ion-laden flow electrodes exit the electrode chambers, undergo regeneration of their charge state in an external circuit, and then re-enter the system for continuous desalination [32].

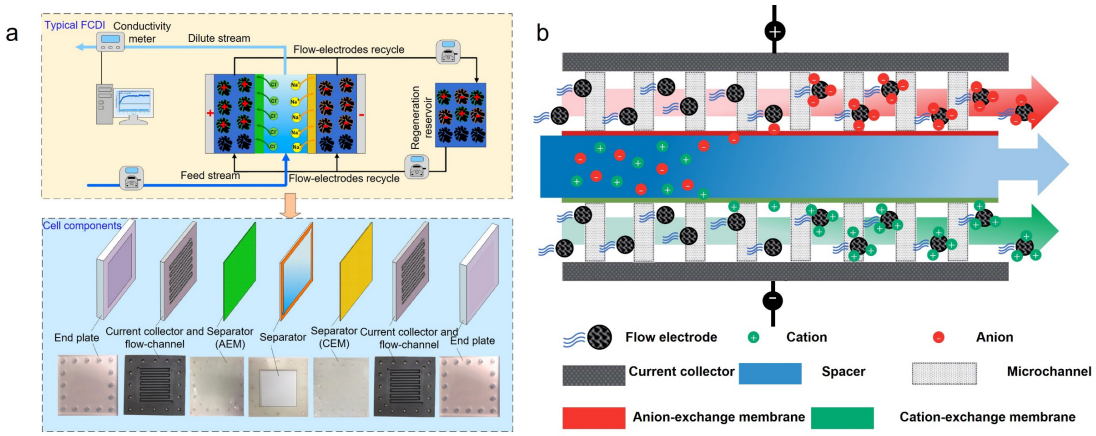

Figure 4. (**a**) Schematic representation of a typical laboratory scale FCDI device and its major components. Photos of the major components are also provided. Reprinted with permission from Ref. [32]. Copyright 2021, American Chemical Society. (**b**) Schematic of the FCDI process. The flowable electrode continuously circulates between the IEM and current collector. Reprinted with permission from Ref. [30]. Copyright 2013, The Royal Society of Chemistry.

Kim et al. [30] pioneered the FCDI system utilizing carbon-based suspensions as flow electrodes. When a voltage is applied between the current collectors of the FCDI cell, electrolyte ions migrate through the IEMs to the flow electrodes and are adsorbed; simultaneously, the ion-saturated electrodes flow through an external circuit for regeneration (Figure 4b). This design eliminates the need for the electrode desorption step required in conventional CDI to release adsorbed ions, ensuring continuous desalination. By adjusting the flow velocity and circulation mode of the electrodes, the process can be optimized for treating feed water of varying salinities, such as seawater. Studies demonstrate that the FCDI system achieves a total dissolved solids (TDS) removal capacity of up to 35,000 $mg \cdot L^{-1}$, significantly surpassing the technical limitations of traditional CDI. Furthermore, spent flow electrodes can be efficiently recovered via simple gravitational sedimentation with minimal material loss.

3.1. FCDI Electrode

FCDI faces key challenges in desalination and wastewater treatment:(i) Limited electron transport between dispersed electrode particles; (ii) Elevated viscosity at high particle loadings, resulting in clogging and leakage risks within electrode channels [92–94]. Addressing these limitations is crucial for enhancing the desalination efficiency and operational stability of FCDI systems. Recent research strategies focus on optimizing flow electrode composition, improving current collector design, and implementing magnetic field-assisted particle alignment. These approaches not only enhance interfacial charge transfer processes but also improve the overall electrical conductivity and mobility of the electrodes, thereby significantly boosting system performance.

3.1.1. Particle Size

The electrode constitutes the most critical and extensively studied component in FCDI systems. Unlike other CDI technologies, FCDI utilizes flowable slurry electrodes, which inherently suffer from incomplete interparticle contact, compromised electrical conductivity, and susceptibility to channel clogging. To address these limitations, initial research efforts focused on modulating the particle size within the slurry. AC serves as the primary material for such electrodes. Zaviska et al. [95] produced fine activated carbon (FAC) particles via ball-milling of AC powder. Morphological comparisons between AC and FAC are presented in Figure 5a,b, revealing significantly reduced particle dimensions and enhanced contact area in the milled material. This particle size reduction, coupled

with improved pore accessibility (Figure 5c), resulted in superior desalination performance compared to pristine AC. Notably, although smaller slurry particles typically increase viscosity and energy consumption, experimental data demonstrated only a marginal increase in energy demand for FAC milled for 90 min (Figure 5d). To systematically investigate the influence of particle size on FCDI viscosity and desalination efficiency, the team evaluated FCDI performance using AC with varying particle sizes. The findings indicate that finer AC particles enhance desalination capacity by increasing the available contact surface area, while larger particles improve slurry fluidity by reducing pressure drop [96]. Consequently, a broader particle size distribution enables an optimal trade-off between desalination performance and energy consumption.

This principle exhibits universal applicability, extending beyond single-component AC systems to diverse carbon-based materials. Through systematic investigation of five carbon-based electrodes in both individual and hybrid configurations, Xue et al. [97] uncovered intrinsic structure-property relationships governing desalination performance and energy efficiency. Experimental results demonstrate that nano-scale electrode materials-carbon black (CB), multi-walled carbon nanotubes (MWCNTs), and graphene nanoplatelets (GNPs)-at 2 wt% carbon loading significantly outperformed micro-scale counterparts (AC and carbon fibers, CF). Owing to distinct spatial configurations among the three nano-materials, hybrid electrodes demonstrated a distinct performance hierarchy: AC + MWCNTs/GNPs > AC + CB > pristine AC systems.

3.1.2. Redox Mediators

Incorporating redox mediators (RMs) represents one of the simplest and most efficient technical approaches for modifying flowable slurry electrodes [98,99]. The core mechanism of introducing RMs into FCDI systems lies in their ability to function as "electron shuttles" through highly efficient and reversible redox reactions at the electrode interface. This significantly enhances electron transfer efficiency between suspended carbon materials and current collectors, thereby effectively reducing the system's interfacial charge transfer resistance and operating voltage. This mechanism synergizes with carbon materials (e.g., AC, carbon nanotubes (CNTs)) or conductive polymers (e.g., PEDOT:PSS) to establish highly efficient electron-ion hybrid conduction pathways [100–102]. The resulting synergistic effects markedly enhance charge transfer kinetics and interfacial ion transport, leading to substantially reduced energy consumption, significantly improved desalination rates, and notably enhanced operational stability. Chen et al. [103] systematically evaluated the impact of four commonly used RMs on FCDI performance. As shown in Figure 5e, the addition of 10 mM $K_3[Fe(CN)_6]$ to the flowing electrode significantly enhanced desalination efficacy. Under carbon loadings of 5% and 10%, the average salt removal rate (ASRR) increased by 267.2% and 262.3%, respectively. Mechanistic studies revealed that the hexacyanoferrate undergoes the $[Fe(CN)_6]^{3-/4-}$ redox reaction at the current collector surface. This electron transfer process induces the migration of charged species across the IEM into the electrode chamber, where they participate in interfacial electrochemical reactions with the AC: $[Fe(CN)^6]^{4-} + AC \rightarrow [Fe(CN)_6]^{3-} + AC^-$. This reaction drives the formation of an EDL on the AC surface, enabling efficient capture of sodium ions via electrostatic adsorption. Figure 5f further corroborates that the indirect charge transfer initiated by $K_3[Fe(CN)_6]$ is the dominant mechanism governing the Na^+ adsorption process. Rajendran et al. [104] conducted a similar study, systematically investigating the effect of mixing high- and low-surface-area AC with redox couples on FCDI desalination performance. The results demonstrated that combining high-surface-area AC with the ferri/ferrocyanide redox couple significantly enhanced desalination efficiency, achieving 76.38%.

While vanadium-based, ferricyanide, and organic molecular redox additives have been shown to enhance FCDI desalination rates, Wessling et al. [105] noted concerns regarding secondary pollution and high costs associated with these systems. Addressing these limitations, they proposed two iron-based redox couples: iron chloride and ferric citrate. Their investigation revealed that an AC slurry incorporating iron chloride achieved twice the desalination capacity of a conventional AC slurry. Furthermore, water treated using a flow electrode modified with ferric citrate exhibited a final pH closer to drinking water standards compared to other systems.

Furthermore, in flow-electrode capacitive deionization systems, the strategic matching of redox mediators with specific pollutant characteristics is essential for achieving efficient treatment. The $Fe(CN)_6^{3-/4-}$ or I^-/I_3^- systems, known for their high reversibility and low toxicity, demonstrate excellent performance in removing conventional ions [104,106–108]. For heavy metal contaminants, mediators such as quinones and Fe-EDTA exhibit distinct advantages due to their exceptional complexation capability and selective adsorption characteristics [109,110]. Meanwhile, organic pollutants can be effectively treated using mediators like reactive oxygen species (ROS), hydro-carbons, aromatics, and amines, which provide outstanding conductivity and catalytic oxidation functions [111]. This precise alignment between pollutant properties and mediator functionality significantly enhances the system's treatment efficiency and selectivity for specific contaminants.

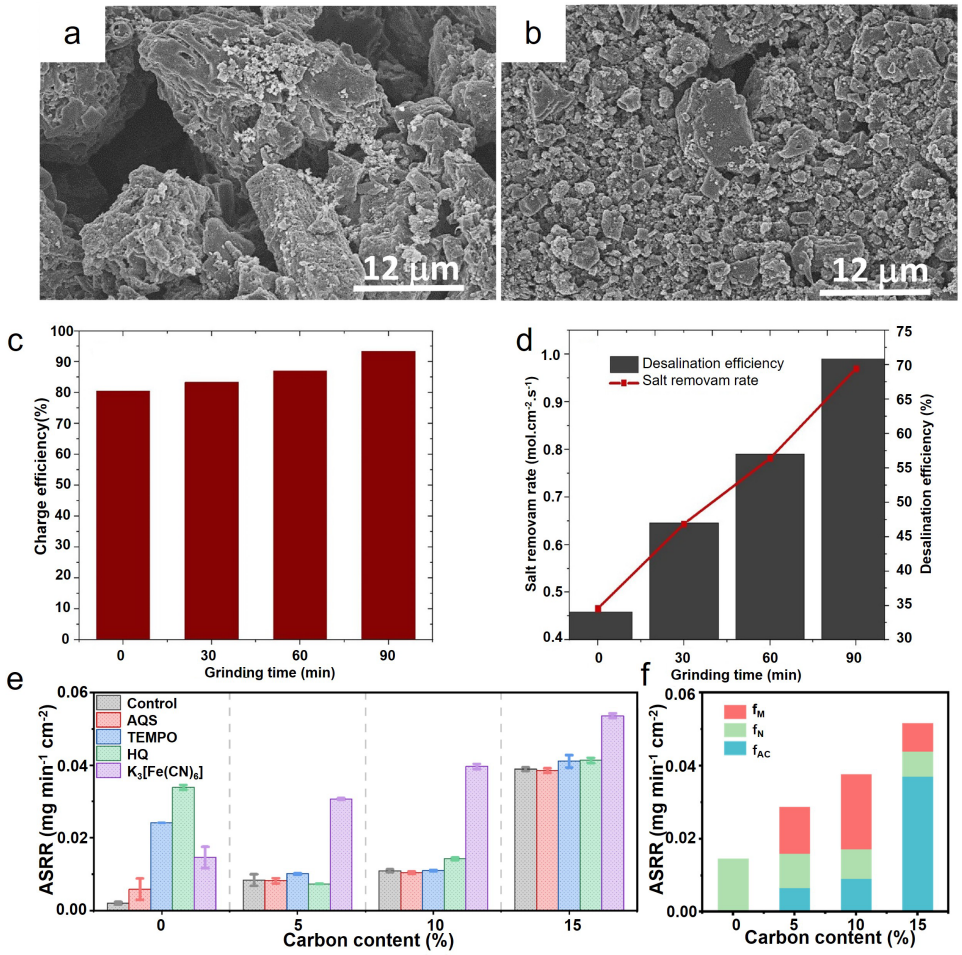

Figure 5. SEM images of (**a**) pristine AC and (**b**) FAC after 90 min grinding. (**c**) Salt removal rate and desalination efficiency and (**d**) charge efficiency of AC and FAC at different grinding time. Reprinted with permission from Ref. [95]. Copyright 2022, Elsevier. (**e**) ASRR of the FCDI cell with the flow electrodes containing different RMs and carbon contents. "Control" represents the flow electrodes that did not contain RMs. [RM] TOT = 10 mM, where RM = AQS, TEMPO, HQ or $K_3[Fe(CN)_6]$. (**f**) Contributions of different pathways to ASRR. f_{AC} is the ion migration rate induced by direct charge transfer process between the graphitic current collector and the ACs, f_N stands for the direct ion migration rate by the redox reaction of RMs, and f_M represents ion capture rate due to the indirect charging of the carbon particles. Reprinted with permission from Ref. [103]. Copyright 2022, Elsevier.

3.1.3. Materials

In FCDI systems, flow electrodes are predominantly composed of carbon-based materials. Consequently, research efforts have primarily focused on modifying and functionalizing these carbon-based components. Zhang et al. [112] fabricated a porous polyaniline-activated carbon (pPANI-AC) composite flow electrode via in-situ polymerization. This design leverages the pseudocapacitive effect of porous polyaniline while simultaneously enhancing the accessibility of AC pores and surfaces, thereby optimizing ion transport pathways. Structural optimization significantly increased the material's SSA (from 213.5 to 616.1 $m^2 \cdot g^{-1}$) and capacitance (from 93 to 178 $F \cdot g^{-1}$), while substantially reducing the viscosity of the electrode suspension (from 127 to 21 Pa·s). Collectively, these performance enhancements resulted in a 70% improvement in the system's desalination efficiency.

CNTs serve as ideal modifiers for flow electrodes owing to their exceptional electrical conductivity, high SSA, and structural tunability [113,114]. Linkhorst et al. [115] fabricated porous microscale poly(3,4-ethylenedioxythiophene):poly(styrenesulfonate) (PEDOT:PSS)-CNT composite flow electrodes by integrating PEDOT:PSS with CNTs. The composite exhibits intrinsic porosity, flexibility, low density (1.01–1.18 $g \cdot cm^{-3}$), and pronounced hydrophilicity. As depicted in Figure 6a, after 1-h sedimentation, the 1.5 wt% PEDOT:PSS-CNT suspension demonstrated a substantially higher volumetric fraction (60–70 vol%) compared to 7.5 wt% AC. This enhanced packing density promotes greater interparticle contact probability, thereby improving electrode utilization efficiency. Viscosity measurements in Figure 6b reveal a continuous decrease in electrode viscosity with increasing CNT content. At 40 wt% CNT loading, the viscosity (~80 mPa·s) approached that of 7.5 wt% AC

slurry (~100 mPa·s). This characteristic confers exceptional pumpability-maintaining favorable fluidity even when particle concentrations significantly exceed the percolation threshold-representing a critical advantage over conventional AC materials. Furthermore, Figure 6c demonstrates that PEDOT:PSS-CNT achieves a remarkable SAC of 955 mg·g^{-1}, surpassing AC by 8–10 times and exceeding the highest documented AC performance records. The primary objective of material compositing is to synergistically combine the merits of individual components while compensating for their inherent limitations, thereby achieving a "whole greater than the sum of its parts" effect. Wang et al. [116] developed an AC/(CB + CNT) ternary composite slurry by incorporating both CB nanoparticles and CNT nanoparticles into an AC-based slurry, leveraging CNTs interparticle bridging capability and CB filling strategy. In comparison to AC/CB and AC/CNT systems (Figure 6d), spherical CB particles exhibited significant agglomeration around AC particles, whereas tubular CNTs formed entangled clusters between AC particles. This distinctive point-line-plane connectivity morphology creates enhanced synergistic sites that accelerate charge percolation network development within the slurry. Since charge transfer primarily involves electron transport from electrode current collectors to active particles and ion migration from electrolytes to particle micropores, these processes generate corresponding responses in electronic current density (I_e) and ionic current density (I_{ion}). Computational fluid dynamics (CFD) simulations (Figure 6g) revealed that the Type IV slurry demonstrated significantly expanded high-I_e and high-I_{ion} regions compared to other formulations, indicating superior charge transfer capabilities. This enhancement stems from CNT particles serving dual functions: connecting AC particles to current collectors while bridging and filling interparticle spaces, thereby establishing efficient point-line-plane contact pathways. Furthermore, the extensive external surface area of CNTs acts as an additional ionic buffer reservoir, providing lower-resistance ion transport paths through surface capacitance effects. Experimental measurements (Figure 6e) demonstrated that the AC/(CB + CNT) slurry achieved an average salt removal rate (ASAR) of 4.41 μmol cm^{-2} min^{-1} under sustained 1.6 V operation, corresponding to 4.45-, 1.79-, and 1.32-fold improvements over pure AC, AC/CB, and AC/CNT slurries, respectively. Moreover, the AC/(CB + CNT) slurry exhibited exceptional desalination stability during prolonged operation (Figure 6f), maintaining a CE of approximately 96.74% and a normalized concentration (C/C_0) of 0.21. Zhao et al. [117] constructed a flexible and continuous three-dimensional conductive network (HCS@CNT) by integrating hollow carbon spheres (HCS) with CNTs. Due to the inherent excellent fluidity of HCS and its unique spherical node structure, this composite design effectively prevents CNT agglomeration, thereby significantly enhancing their bridging function within the three-dimensional framework. Furthermore, the CNTs act as conductive "bridges" within the structure, facilitating more efficient and frequent electron transfer and ion migration. However, it is worth noting that the current manufacturing cost of the HCS@CNT composite remains substantially higher than that of conventional AC materials, posing a major impediment to its commercial-scale implementation.

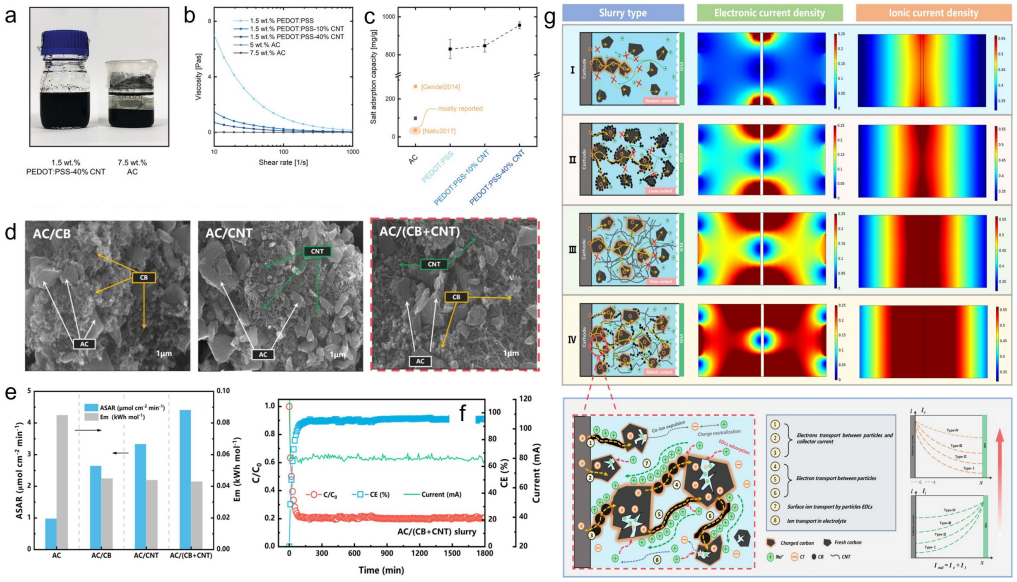

Figure 6. (**a**) Photograph of a PEDOT:PSS-CNT and AC flow electrode after sedimentation. (**b**) Viscosity of PEDOT:PSS-CNT and electrochemically comparable AC flow electrodes measured in a plate-plate rheometer setup. (**c**) Comparison of the SAC of PEDOT:PSS-CNT flow electrodes of various CNT concentration with an AC slurry. Reference values from literature are presented in orange. Reprinted with permission from Ref. [115]. Copyright 2023, Wiley-VCH. (**d**) SEM images of AC/0.2 wt% CB, AC/0.2 wt% CNT, and AC/0.2 wt% (CB + CNT). (**e**) the calculated ASAR and Em. (**f**) The temporal profiles of C/C_0, CE, and I for AC/(CB + CNT) flow

electrodes during long-term operation in single-pass/SCC mode within the FCDI system. (**g**) Schematic diagrams illustrating electron/ion transport processes and electronic/ionic current density distribution plots for AC (type-I), AC/CB (type-II), AC/CNT (type-III), and AC/(CB + CNT) (type-IV). Analysis of the enhanced charge transport mechanism in AC/(CB + CNT) (type-IV). Reprinted with permission from Ref. [116]. Copyright 2023, Elsevier.

Owing to its excellent intrinsic conductivity and low cost, CB is considered a highly promising alternative material. However, CB particles exhibit strong agglomeration tendencies in solution, substantially diminishing their effective SSA and active sites. To mitigate this limitation, Peng et al. [118] implemented surface modification of CB particles using Direct Blue (DB) molecules, effectively suppressing CB agglomeration and sedimentation. Given that sulfonate groups in DB significantly enhance surface hydrophilicity, this approach concurrently improves both dispersion stability within flow electrodes and system-level energy conversion efficiency. Experimental results demonstrate that under optimized conditions (DB:CB mass ratio = 1:500, cell voltage = 1 V), the modified electrode achieved an ASRR of 53.43 $\mu g \cdot cm^{-2} \cdot min^{-1}$ during treatment of 2900 ppm saline water, with corresponding salt removal efficiency (SRE) of 78.5% and coulombic efficiency of 93.17%.

Owing to its low cost, environmental compatibility, abundant availability, porous structure, and excellent electrical conductivity, biomass is recognized as a highly promising electrode candidate material. The development of biomass-derived flow electrodes further aligns with carbon neutrality strategic objectives. Yao et al. [119] synthesized pinewood-derived porous carbon (PPC) with hierarchical pore structures through high-temperature carbonization combined with KOH activation using pinewood powder as the precursor. When evaluated in FCDI systems, the PPC electrode exhibited exceptional desalination performance: an ASAR of 23.3 $\mu g \cdot cm^{-2} \cdot min^{-1}$ and desalination efficiency reaching 98.96%. These results unequivocally validate the high-efficiency salt removal capability and practical utility of biomass-derived flow electrodes in real-world applications such as water treatment. Moreover, the development of biomass-based flow electrodes contributes to carbon neutrality initiatives, thereby offering dual environmental benefits through climate change mitigation and environmental crisis alleviation.

MOFs demonstrate distinctive advantages as electrode materials in CDI desalination and wastewater treatment applications, owing to their ultrahigh SSA, tunable porosity, and precisely designable pore structures. Capitalizing on these attributes, Liu et al. [120] developed a porous carbon-based flow electrode (C-MOF@G) through surface modification of MOF-5 with graphene oxide (GO). This modification strategy not only preserved electrode structural integrity but also significantly enhanced the material's SSA. Under optimized operating conditions (voltage: 1.2 V, flow rate: 20 $mL \cdot min^{-1}$, carbon content: 4 wt%, NaCl concentration: 1 $g \cdot L^{-1}$), the C-MOF@G electrode achieved a salt removal rate of 68.4 $\mu g \cdot cm^{-2} \cdot min^{-1}$-1.8-fold and 8.7-fold higher than pristine C-MOF and AC electrodes, respectively. Given the structural homology between PBA coordination polymers and MOFs, the team innovatively constructed a NiHCF@CNTs composite flow cathode by bridging nickel hexacyanoferrate (NiHCF) with carbon nanotubes. This composite exhibited sustained desalination stability throughout 20 consecutive operational cycles [121].

Future research should focus on developing low-cost materials and addressing low energy consumption. Integrating multi-scale simulations and in-situ characterization techniques will deepen the understanding of interfacial charge transfer mechanisms, advancing FCDI technology toward high efficiency and sustainability.

3.1.4. Magnetic Field-Coupled Magnetic Electrodes

Magnetic FCDI technology significantly enhances desalination efficiency through the innovative integration of magnetic field regulation. This technology employs composite flow electrodes such as magnetic carbon (MC), where magnetic materials synergistically interact with functionalized carbon materials. Wu et al. [122] pioneered the magnetic field-assisted FCDI system. By applying external magnetic fields on both sides of the electrode chambers, they achieved oriented enrichment of magnetic carbon particles near the current collectors, fully activating their adsorption sites and realizing over 100% improvement in desalination performance. However, particle agglomeration induced by high salt concentrations led to increased pumping energy consumption and reduced system stability. To overcome this limitation, the team developed an optimized magnetic array design (Figure 7a): magnets were uniformly arranged along the flow channel to create alternating magnetic/non-magnetic regions. Using core-shell structured MC as a conductive additive, the flow electrode was guided to form a high-concentration layer near the current collectors within magnetic zones, while recovering a uniformly dispersed state upon entering non-magnetic zones (Figure 7b). Experiments confirmed this design boosted the desalination rate by 120% in low carbon-loading systems (1.0–2.0 wt%), maintaining a stable ASRR of 0.35 $\mu mol \cdot cm^{-2} \cdot min^{-1}$ at 1.2 V, effectively balancing desalination efficiency and energy consumption [123]. Addressing the issue of magnetic component separation in core-shell MC during long-term cycling, the team further designed a novel

Fe_3O_4@C structure: encapsulating Fe_3O_4 nanoparticles within an AC matrix (Figure 7c). After 20,000 cycle testing, the Fe_3O_4@C electrode maintained stable current density (j), ASRR, and CE (Figure 7d). Post-cycling SEM analysis revealed intact particle morphology without carbon layer detachment (Figure 7e,f). XPS characterization (C 1s, Fe 2p, O 1s spectra, Figure 7g–i) confirmed the chemical structure stability of the material during continuous operation, providing reliable assurance for the long-term operation of magnetic FCDI systems [124].

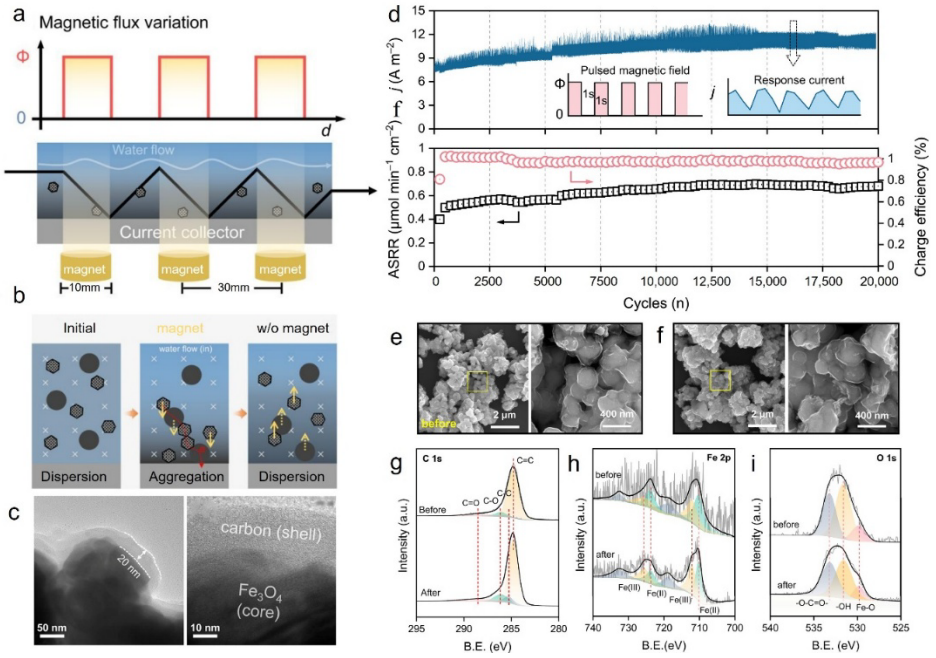

Figure 7. (**a**) Magnetic flux variation and MC transport in flow channel. (**b**) Schematic illustration of the effects of MC on flow electrodes. Reprinted with permission from Ref. [123]. Copyright 2022, Elsevier. (**c**) TEM images of Fe_3O_4@C. (**d**) Variations in current density (j), ASRR, and CE of the magnetic FCDI system under pulsed magnetic field (PMF) mode. (**e**,**f**) SEM images and (**g**–**i**) XPS spectra of Fe_3O_4@C samples before and after 20,000 cycles. Reprinted with permission from Ref. [124]. Copyright 2022, Elsevier.

3.2. Current Collectors

In FCDI systems, current collectors are typically fabricated from highly conductive materials, serving dual critical functions: providing physical support to guide flow electrode movement while establishing efficient charge-transfer pathways between external power sources and active materials in flow electrodes. Although conventional graphite collectors exhibit high electrical conductivity and large SSA, they present significant challenges during prolonged operation. These materials are susceptible to mechanical wear from flow electrode friction and oxidation reactions with environmental components. Such issues not only reduce material utilization efficiency but also frequently trigger electrode deposition. This phenomenon severely compromises operational stability, impedes effective ion transport, and ultimately impairs CDI system performance. To address limitations of conventional graphite current collectors, Zhao et al. [125] developed a polyaniline-graphite composite current collector (PGP-CC) via material modification. The incorporated polyaniline exhibits high electrical conductivity and notable pseudocapacitance, establishing additional conductive active sites within the composite framework. These enhanced charge transport pathways facilitate more efficient electron transfer, improving charge transfer efficiency by 18.7%. Significantly, the novel composite mitigates electrostatic repulsion between AC particles, reducing electrode deposition by 15%. This advancement not only decreases maintenance costs but also enhances desalination performance and operational stability of FCDI systems, demonstrating superior practicality compared to conventional configurations.

The structural design of current collectors critically governs their electrochemical performance. Systematic investigations reveal inherent limitations in 2D collectors concerning charge transfer kinetics and electric field distribution: planar geometry constrains charge transport pathways, reduces effective field coverage, and restricts charge-transfer interfaces, thereby diminishing system efficiency. In contrast, 3D architectures effectively mitigate these deficiencies by enhancing field homogeneity and expanding charge-transfer surface area. As demonstrated in Figure 8a–d, Zhao et al.'s carbon-coated 3D nickel foam collector enables electron transfer to substantially more AC particles within flow channels compared to 2D configurations, exhibiting stronger electric field intensity for

broader charge delivery. Quantitative analysis confirms the 3D collector's charge-transfer area (11.5%) significantly surpasses that of 2D counterparts (8.99%), facilitating effective charging of more AC particles. This carbon-coating strategy optimizes electric field distribution through extended charge-transfer interfaces, enhancing FCDI desalination performance by 15.3%. Further studies (Figure 8e) demonstrate pore density profoundly influences performance: decreasing pore size (20 ppi → 35 ppi) increases charge-transfer area from 11.5% to 43.4%, verifying enhanced charge delivery through expanded interfacial contact at higher pore densities. However, the inactive zone proportion concurrently rises from 5.56% to 8.95%, indicating excessive pore density generates non-conductive regions that may impede hydrodynamic flow and reduce carbon slurry utilization efficiency. These findings underscore the necessity to balance maximized charge-transfer area against minimized inactive zones, with 30 ppi identified as the optimal pore density. Notably, the system maintains stable desalination performance when treating actual seawater samples from the Yellow Sea and South China Sea (Figure 8f,g), demonstrating significant potential for large-scale desalination applications [126]. Building upon this principle, Zhou et al. [127] engineered a three-dimensional titanium mesh current collector (3D-TM). As structurally illustrated in Figure 8h, the 3D-TM significantly enhances charge-transfer area through a unique cross-stacking design. This configuration simultaneously induces turbulent flow effects, promoting electron transfer, charge penetration, and ion migration processes. A representative 20-mesh 3D-TM with 12 stacked titanium layers achieves an average desalination rate of 5.06 μmol·cm^{-2}·min^{-1} at 2.0 V with 92.9% CE. Remarkably, the system maintains over 76.4% desalination performance after 100 consecutive cycles, validating the exceptional cycling stability of the 3D-TM FCDI system.

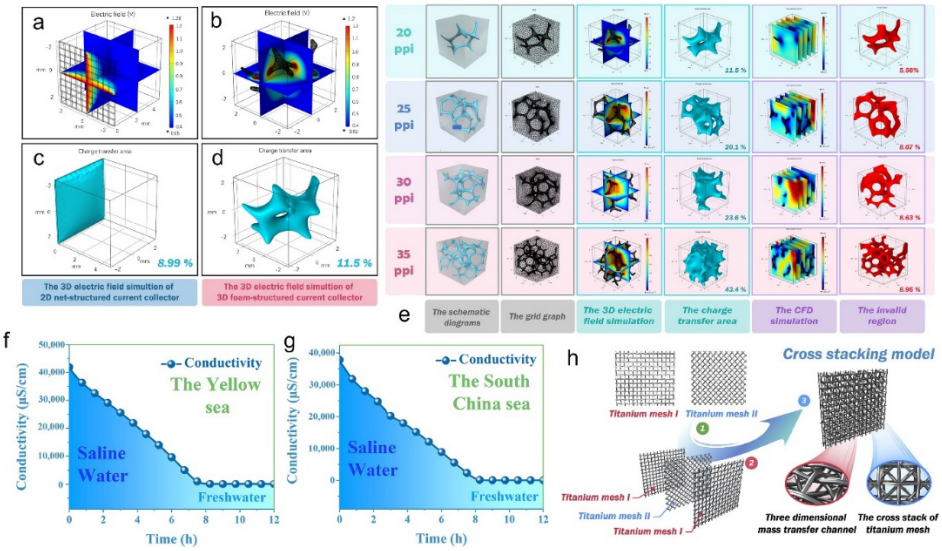

Figure 8. 3D electric field simulation of (**a**) 2D planar structured and (**b**) 3D foam-structured current collector; The charge transfer area of (**c**) 2D planar structured and (**d**) 3D foam-structured current collector. (**e**) Schematic diagrams, grid graphs, 3D electric field simulation plots, charge transfer area plots, CFD simulation plots, and inactive zone plots of the 3D foam current collector model with 20–35 μm pore size in 3D electric field and CFD simulations. (**f**) The long-term desalting test of real seawater sample from Yellow Sea and (**g**) South China Sea in carbon coated nickel foam flow-electrode capacitive deionization (CF-FCDI) device. Reprinted with permission from Ref. [126]. Copyright 2022, Elsevier. (**h**) Cross-stacked configuration of the 3D-TM current collector. Reprinted with permission from Ref. [127]. Copyright 2024, Elsevier.

Structural refinement necessitates exploration of more suitable electrode configurations, where peak performance is contingent upon optimal compatibility between flow electrodes and current collectors. Yu et al. [128] investigated the synergistic interplay between collector architecture and flow electrodes, constructing a 3D-FCDI system employing porous titanium foam as the collector and rectorite (Rec) as the flow electrode. To substantiate the superiority of Rec electrodes, comparative analysis was performed against AC and CB counterparts. Results demonstrate that under 1.8 V applied voltage with 5 wt% electrode concentration in SCC mode, the Rec electrode achieves an ASAR of 11.74 μg·cm^{-2}·min^{-1}, exhibiting markedly enhanced desalination performance.

Beyond optimizing collector materials and structures, the design of flow electrode channels is equally critical. Conventional collectors primarily employ straight or parallel-connected channels, yet such simplistic designs exhibit inherent limitations: they inevitably cause non-uniform solution distribution. This flow field heterogeneity further reduces ion-electrode contact efficiency, impeding optimal FCDI performance. Inspired by the hydrodynamic principles governing liquid flow electrodes, Zhang et al. [129] innovatively incorporated

Archimedean spiral channels (Figure 9a,b). This configuration enables more uniform flow velocity distribution and prolongs fluid residence time, significantly enhancing desalination efficiency. Subsequently, novel channel designs including mosquito-repellent incense-shaped channels, double Fermat spirals, and hexagonal honeycomb dynamic channels have been proposed (Figure 9c–f) [130–132]. Pawłowski et al. [133] further revealed that channels inducing flow perturbations effectively reduce flow electrode viscosity, thereby improving fluidity. This insight provides a viable approach to mitigate channel clogging. With advancing research, design principles for flow electrode channels are being systematically refined.

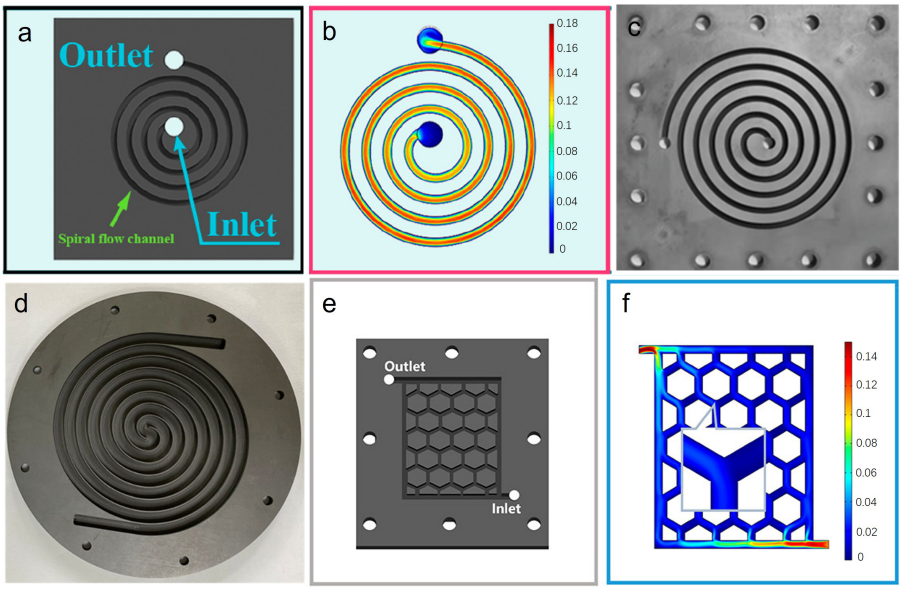

Figure 9. (**a**) a 2D schematic of the spiral flow channel model and (**b**) velocity distribution of carbon paste. Reprinted with permission from Ref. [129]. Copyright 2022, American Chemical Society. (**c**) current collector with spiral mosquito-repellent incense-shaped channel. Reprinted with permission from Ref. [131]. Copyright 2022, American Chemical Society. (**d**) current collector with dual Fermat spiral flow channels. Reprinted with permission from Ref. [130]. Copyright 2023, American Chemical Society. (**e**) 2D schematic of the hexagonal honeycomb-shaped flow channel and (**f**) velocity distribution of carbon paste. Reprinted with permission from Ref. [132]. Copyright 2023, American Chemical Society.

4. Novel Design of CDI

A prominent trend persists in current CDI selective separation research: predominant focus remains on developing selective materials. While these materials undeniably play a critical role in enhancing CDI performance, this emphasis has led to prolonged neglect of system design considerations. In reality, CDI architectural design constitutes an equally vital determinant of overall functionality. System optimization expands application scenarios, reduces energy consumption, and improves desalination efficiency, thereby enabling multifaceted enhancement of CDI performance.

Liu et al. [134] revealed that IEM structures critically influence desalination performance: the significantly higher diffusion coefficient of Cl^- versus Na^+ induces a thicker ion depletion layer near cation exchange membranes (CEMs) (due to rapid Cl^- migration) and a more pronounced ion enrichment layer (resulting from restricted Na^+ counter-migration). Leveraging this phenomenon, the team developed a dual-channel FCDI system (CAC-FCDI, Figure 10a) featuring an asymmetric architecture with dual CEMs sandwiching an AEM. This configuration accelerates adsorption kinetics in flow electrodes, enhancing desalination efficiency, particularly for NaCl solutions or seawater where Na^+/Cl^- exhibit divergent diffusion coefficients.

Xiao et al. [135] engineered a four-chamber flow-electrode capacitive deionization system (F-FCDI, Figure 10b) that directly channels removed metal ions into concentration chambers, bypassing flow electrodes. This mechanism prevents performance degradation caused by metal ion adsorption and reduction on AC. Experimental results demonstrate successful concentration of 2000 mL copper ions (Cu^{2+}) solution (initial concentration: 100 ppm) to 50 mL after 48-h cycling (enrichment factor: 28.5). The system also exhibits effective removal capabilities for lead (Pb^{2+}), cadmium (Cd^{2+}), and cobalt (Co^{2+}) ions. Wang et al. [136] proposed an innovative tri-channel CDI configuration where saline water flows directly through electrodes, maximizing salt ion-electrode contact efficiency to ensure high-performance desalination.

Wang et al. [137] developed an innovative two-stage flow-electrode system (TS-FCDI, Figure 10c) that integrates stationary and flow electrodes. This synergistic coupling substantially expands the electroactive interfacial area, thereby enhancing ion removal efficiency while improving overall electrochemical performance. Remarkably, the system attains an ASRR of 113 $\mu g \cdot cm^{-2} \cdot min^{-1}$, demonstrating twice the desalination capacity of conventional FCDI systems.

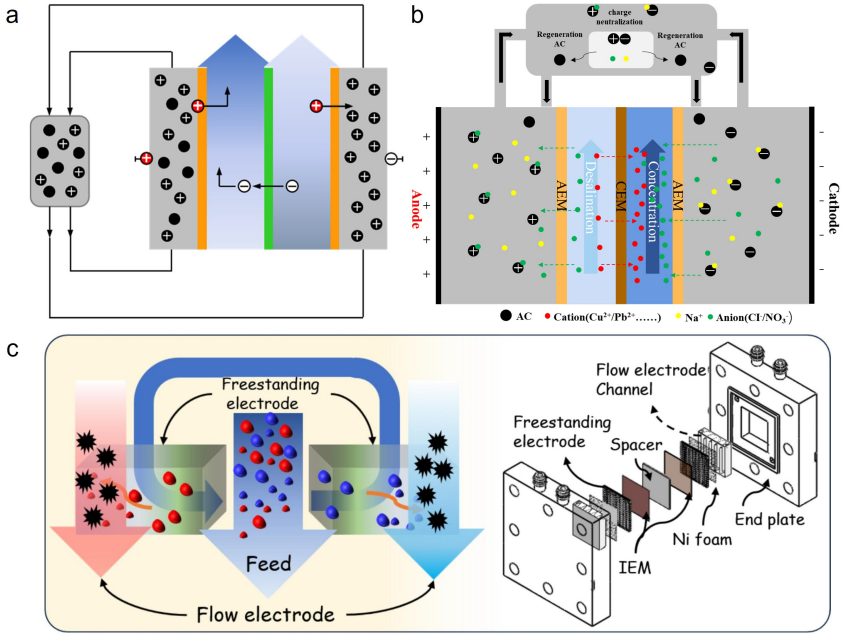

Figure 10. Schematic diagrams of (**a**) the CAC-FCDI system. (**b**) the F-FCDI system, and (**c**) the TS-FCDI system.[134,135,137]. Reprinted with permission from Ref. [134]. Copyright 2023, Elsevier. Reprinted with permission from Ref. [135]. Copyright 2023, Elsevier. Reprinted with permission from Ref. [137]. Copyright 2024, Elsevier.

5. Removal of Other Substances

5.1. Removal of Inorganic Ions

Common inorganic ions in aquatic environments encompass not only Na^+ but also cations such as Li^+, Ca^{2+}, and Mg^{2+}, along with anions including Cl^-, PO_4^{3-}, and SO_4^{2-}, which collectively form the fundamental ionic composition of natural water bodies. Li^+, as a strategic emerging resource, poses a dual challenge for water treatment technologies-its accumulation reflects the impact of modern industrial development, requiring both control of its environmental concentration and the realization of its recovery potential as a valuable resource [138,139]. Meanwhile, excessive PO_4^{3-} serves as a key driver of water eutrophication, stimulating algal blooms, depleting dissolved oxygen, and disrupting aquatic ecosystem balance [140]. Consequently, the effective management and selective removal of these common inorganic ions, particularly the resource-oriented recovery of Li^+ and advanced purification of PO_4^{3-}, represents a core challenge and critical research direction for the practical application of CDI technology.

Li et al. [141] developed a composite electrode featuring a core-shell architecture, with nickel hexacyanoferrate as the core and λ-MnO_2 as the shell. This design demonstrated outstanding lithium extraction performance, achieving a high adsorption capacity of 43.51 $mg \cdot g^{-1}$, a fast adsorption rate of 8.1 $mg \cdot g^{-1} \cdot min^{-1}$, and a low energy consumption of 0.86 $Wh \cdot g^{-1}$. The electrode also exhibited remarkable ion selectivity, with separation factors for Li^+ over Na^+ and Mg^{2+} reaching 68.7 and 21.0, respectively. These superior properties are attributed to the synergistic effect at the core-shell interface, which facilitates rapid lithium-ion migration and enhances structural stability, as evidenced by a high capacity retention of 78.4% after 40 cycles in a real brine environment. In a parallel development focusing on material fundamentals, Shetty et al. [142] pioneered the use of covalent organic frameworks as cathode materials for electrochemical lithium recovery via hybrid capacitive deionization. They engineered a two-dimensional COF, termed Tta-Dfp, with a precisely controlled distribution of nitrogen species, including pyridine, imine, and triazine motifs. This nitrogen-rich framework delivered a lithium uptake capacity of 15.7 $mg \cdot g^{-1}$ and a lithium selectivity of approximately 80% against competing ions. Furthermore, it showed exceptional electrochemical stability, retaining 97.7% of its initial capacitance after 500 charge-discharge cycles. Experimental data combined with density functional theory calculations revealed that the polarized nitrogen sites within the framework significantly enhance the electrostatic interaction with lithium ions,

underpinning the high selectivity and performance. To tackle the particularly difficult separation of lithium from brines with high magnesium-to-lithium mass ratios, Zhou et al. [143] designed a novel four-stage ion-distillation flow-electrode capacitive deionization system. This device integrates commercial monovalent selective cation exchange membranes with multiple flow-electrode channels. The multi-stage configuration exponentially amplifies the intrinsic selectivity of a single membrane, resulting in an exceptionally high Li^+/Mg^{2+} separation factor of up to 76,295.41, an enrichment ratio of 4.95, and a final lithium solution purity of 99.97%, all while maintaining a low energy consumption of 0.21 $kWh \cdot mol^{-1}$. Electrochemical analysis and mathematical modeling validated that the superior performance stems from the faster migration kinetics of lithium ions, which possess a diffusion coefficient 2.83 times greater than that of magnesium ions and a lower diffusion resistance. The practical viability of this system was confirmed by processing a natural salt lake brine, successfully producing battery-grade lithium carbonate with a purity of 99.66%. Collectively, these studies, ranging from molecular-level material design to macro-scale system integration, provide a comprehensive and promising technological pathway for the efficient and sustainable recovery of lithium resources.

Cho et al. [144] systematically modulated the micropore structure, surface charge, and particle size of coconut shell-derived activated carbon through ball-milling treatment. In a symmetric CDI system without an ion-exchange membrane, the modified carbon achieved high selective adsorption of SO_4^{2-} from a mixed SO_4^{2-}/Cl^- solution, with an adsorption ratio (K value) of 2.13-a 36% improvement over the untreated electrode. This result highlights the potential of mechanical modification in enhancing ion sieving and ion replacement kinetics. Yang et al. [145] prepared biochar from lotus leaves and applied it in a flow-electrode capacitive deionization system. Under an initial phosphorus concentration of 20 $mg \cdot L^{-1}$, a removal efficiency of 98.55% was achieved, with the effluent phosphorus concentration falling below 0.3 $mg \cdot L^{-1}$, meeting stringent discharge standards. The phosphorus removal mechanisms involved multiple pathways, including physical adsorption, electrosorption, ion exchange, precipitation, and ligand exchange, demonstrating the promising engineering application of biomass-derived materials in cost-effective and efficient phosphorus removal. Furthermore, Wang et al. [146] developed a ZnFe-PANI/CNT composite electrode that integrates the high affinity of layered double hydroxides with the excellent conductivity of polyaniline/carbon nanotubes. This material exhibited outstanding phosphate removal performance across a broad pH range (3–10), achieving an exceptionally low effluent concentration of 0.095 $mg \cdot L^{-1}$. It also demonstrated strong resistance to ionic interference and remarkable cycling stability, maintaining a removal rate of 77% after 10 adsorption-desorption cycles. With an extremely low system energy consumption of 0.00274 $kWh \cdot g^{-1}$ P, this composite provides a new material foundation for highly selective and energy-efficient phosphorus recovery technologies.

5.2. Removal of Heavy Metals

Heavy metal pollution represents a critical driver exacerbating freshwater scarcity. Industrial effluents discharged from mining, metallurgy, electroplating, and chemical industries commonly contain toxic heavy metals, including Cu^{2+}, Pb^{2+}, Cd^{2+}, uranium (U^{6+}), arsenic (As^{3+}), and chromium (Cr^{6+}) ions, posing significant risks to human health and ecosystems. Among remediation strategies, CDI has emerged as an effective and promising technology for the removal of heavy metal ions from aqueous solutions.

Cu, a prevalent heavy metal pollutant in industrial wastewater, exists as highly toxic divalent Cu^{2+} with significant recovery potential. Recent research prioritizes developing advanced electrode materials for enhanced copper ion removal. Zhang et al. [147] synthesized ZIF-8-derived Co/Fe co-doped porous carbon (CoFe-NC) electrodes demonstrating exceptional Cu^{2+} removal efficiency in CDI systems. Experimental results revealed a selective adsorption capacity of 85.71 $mg \cdot g^{-1}$ for Cu^{2+} in multi-ion solutions, with negligible removal rates for competing ions. The Langmuir isotherm model indicated a theoretical maximum adsorption capacity of 540.8 $mg \cdot g^{-1}$, confirming outstanding removal performance and ion selectivity. Wang et al. [148] fabricated irregular hexagonal CuSe nanosheet electrodes enabling preferential Cu^{2+} adsorption in complex systems via strong coordination interactions between selenium vacancies and Cu^{2+} ions. Notably, these electrodes maintained stable adsorption capacity (>350 $mg \cdot g^{-1}$) across a broad pH range (0.5–4.5), exhibiting robust performance under strongly acidic to neutral conditions-a critical advantage for practical electroplating wastewater treatment.

In chemical industries, Cu^{2+} exhibits strong affinity for functional groups (e.g., amino and carboxyl groups), forming persistent complexes such as Cu(II)-EDTA that resist conventional removal methods. To address this challenge, Wang et al. [149] developed an integrated system by coupling contact electrocatalysis (CEC) with CDI, enabling synchronous complex decoupling and contaminant adsorption. Furthermore, industrial wastewater contains prevalent toxic heavy metal ions including Pb^{2+}, Cr^{6+}, As^{3+}, Cd^{2+}, and U^{6+}, with specific treatment strategies and performance metrics detailed in Table 1.

Table 1. Performance Benchmark of Heavy Metal Removal via HCDI and FCDI Systems.

Cathode	Anode	Target Ion	Adsorption capacity or Efficiency	Feed Concentration	Flow rate ($mL \cdot min^{-1}$)	Electrode Parameter	Voltage (V)	Cyclic Stability Adsorption Retention	Ref.
COOH/AC		Pb(II)	0.11 $mg \cdot g^{-1}$ 69.2%	100 $\mu g \cdot L^{-1}$	5	5 × 5 cm	1.2		[150]
rGO/NCDs	rGO/NCDs	Pb(II)	19.26 $mg \cdot g^{-1}$	5.0 $mg \cdot L^{-1}$	20	4 × 4 cm	1.0	10 93.6%	[151]
PC-ZIF-67	PC-ZIF-67	Pb(II)	117.2 $mg \cdot g^{-1}$	800 $mg \cdot L^{-1}$		D = 40 mm	1.4	10 90%	[152]
MoO_2/C	AC	Pb(II)	157.7 $mg \cdot g^{-1}$	100 $mg \cdot L^{-1}$	40		1.2		[153]
NF/Mn_2CoO_4@MoO_2	graphite	Pb(II)	156.24 $mg \cdot g^{-1}$ 99.9%	50 $mg \cdot L^{-1}$	10	5 × 5 cm	1.4	10 95.94%	[154]
ZAC@VS_2	AC	Pb(II)	239.52 $mg \cdot g^{-1}$ 99.9%	500 $mg \cdot L^{-1}$	6.6	8 × 10 cm	1.2	6 70.16%	[155]
Fe_7S_8@NCNT	AC	Pb(II)	223.1 $mg \cdot g^{-1}$	200 $mg \cdot L^{-1}$	20	4 × 4 cm	1.2	16 91.0%	[156]
TpPa@rGO	AC	Pb(II)	137.8 $mg \cdot g^{-1}$ 99%	100 $mg \cdot L^{-1}$	40	4 × 4 cm	1.2		[157]
N-$Ti_3C_2T_x$	graphite	Pb(II)	99.5%	5.0 $mg \cdot L^{-1}$	20	1 × 1.5 cm	1.5		[158]
AC	NiFe/MoS_2	Cr(VI)	49.71 $mg \cdot g^{-1}$ 99.42%	100 $mg \cdot L^{-1}$	20		1.2	3 81.0%	[159]
V_2AlC-OH_x	AB	Cr(VI)	47.2 $mg \cdot g^{-1}$ 99.0%	150 $mg \cdot L^{-1}$	10	3 × 3 cm	1.4	20 80%	[160]
AC	NiFe-LDH/PPy	Cr(VI)	47.95 $mg \cdot g^{-1}$ 95.89%	100 $mg \cdot L^{-1}$	20		1.2		[161]
Ni-BTC/$Ti_3C_2T_x$	AC	Cr(VI)	124.5 $mg \cdot g^{-1}$ 94.1%	30 $mg \cdot L^{-1}$		2 × 2 cm	4.0		[162]
AC	CoOx/AC	As(III)	0.0163 $mg \cdot g^{-1}$	150 $\mu g \cdot L^{-1}$	1	1 × 1 cm	1.2	10 ＞92.0%	[163]
CNTs-S@Fe_3O_4	CNTs-S@Fe_3O_4	As(III)	0.464 $mg \cdot g^{-1}$ >95%	1.0 $mg \cdot L^{-1}$	10		1.2		[164]
MO-MgAl	MO-MgAl	As(III)	4.366 $mg \cdot g^{-1}$	4.0 $mg \cdot L^{-1}$	5		1.4		[165]
YP-50F	YP-50F	Cd(II)	54%	100 $mg \cdot L^{-1}$	20		2.4		[166]
W-800	W-800	Cd(II) Tl(I)	177 $mg \cdot g^{-1}$ 597.4 $mg \cdot g^{-1}$	500 $mg \cdot L^{-1}$ 500 $mg \cdot L^{-1}$	30		1.2		[167]
AC	AC	U(VI)	265 $mg \cdot g^{-1}$ 99%	360 $mg \cdot L^{-1}$	20		1.2		[168]
OMPAC	OMPAC	U(VI)	58.5 $mg \cdot g^{-1}$ 97.48%	60 $mg \cdot L^{-1}$	20		1.2		[169]
MoS_2-GO/CC	CC	U(VI)	74.38 $mg \cdot g^{-1}$ 94.9%	5.0 $mg \cdot L^{-1}$		1.5 × 1.5 cm	0.9		[170]
UiO-66-NH_2/MXene	UiO-66-NH_2/MXene	U(VI)	229.1 $mg \cdot g^{-1}$	100 $mg \cdot L^{-1}$		1 × 5 cm	1.2	10 95%	[171]

Although modified materials exhibit superior desalination performance and ion selectivity, their practical implementation faces challenges including high manufacturing costs and poor operational stability. For scenarios requiring non-selective removal, adsorbents with broad-spectrum heavy metal affinity emerge as ideal alternatives. To address this need, Li et al. [172] developed Cu^{2+}-modified super activated carbon electrodes for CDI systems. The Cu^{2+} functionalization synergistically optimizes pore structure and surface chemistry, enabling cooperative heavy metal removal via electrostatic adsorption and complexation mechanisms, achieving high removal efficiencies of 95.2% for Pb^{2+}, 93.9% for Cu^{2+}, and 92.1% for Cd^{2+}. Alternatively, Zhang et al. [173] engineered interlayer-tunable two-dimensional titanium carbon oxides (TCOs) by tailoring alkylammonium cation sizes (TMA^+, TEA^+, TPA^+). Three distinct TCOs with progressively expanded interlayer spacing were synthesized: TCOs-TMAH < TCOs-TEAH < TCOs-TPAH (Figure 11a). Galvanostatic charge-discharge (GCD) analysis (Figure 11b) revealed TCOs-TPAH possesses the longest discharge duration, indicating superior capacitive behavior. At a scan rate of 1 $mV \cdot s^{-1}$, TCOs-TPAH delivers a specific capacitance of 166 $F \cdot g^{-1}$ (Figure 11c), outperforming TCOs-TMAH and TCOs-TEAH. This enhancement originates from its expanded interlayer spacing (1.47 nm), which provides optimized diffusion channels for efficient charge transfer and ion transport, endowing the electrode with reinforced charge storage capacity and exceptional cycling stability.

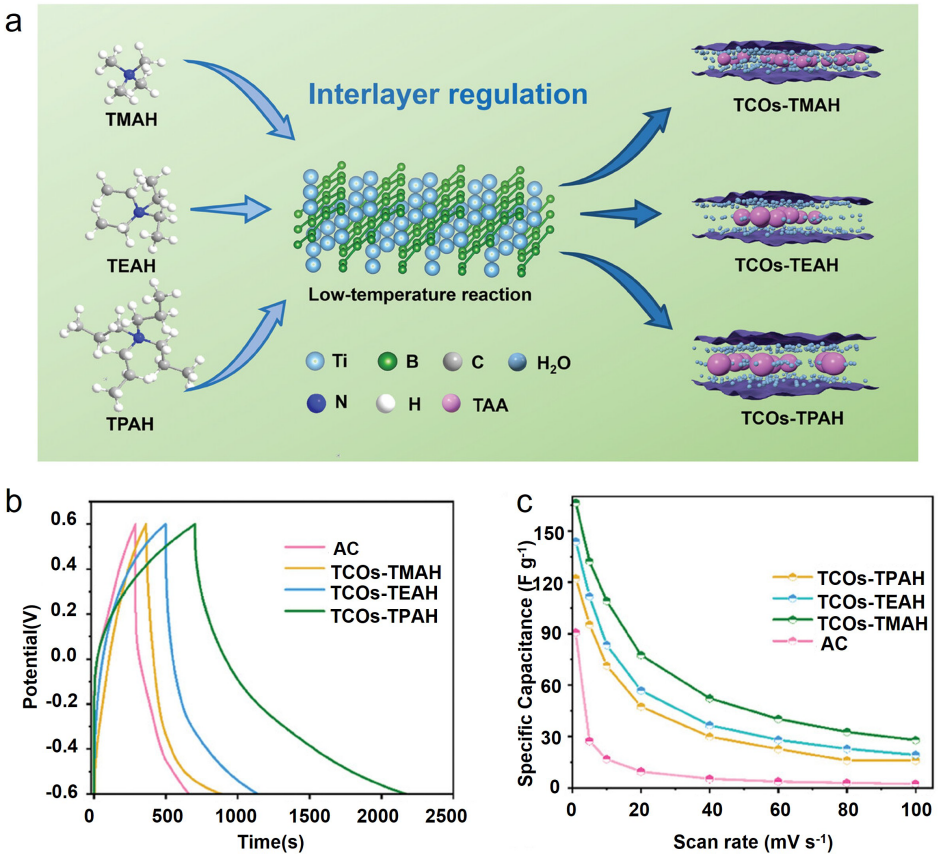

Figure 11. (**a**) Schematic illustrations of TCOs-TMAH, TCOs-TEAH, and TCOs-TPAH preparation processes. Electrochemical performance of TCOs-TMAH, TCOs-TEAH, and TCOs-TPAH in 1.0 mM NaCl solution: (**b**) GCD curves at 0.1 $A \cdot g^{-1}$ current density; (**c**) specific capacitance at scan rates of 1, 5, 10, 20, 40, 60, 80, and 100 $mV \cdot s^{-1}$. Reprinted with permission from Ref. [173]. Copyright 2024, Wiley-VCH.

5.3. Removal of Organic Matter

Current research predominantly concentrates on selective separation of inorganic ions via CDI, whereas organic contaminant removal remains underexplored. This gap primarily stems from inherent incompatibilities between organic compound characteristics and CDI mechanisms. Most organic pollutants (e.g., dyes, pharmaceutical residues, humic acids) exhibit weak polarity or neutrality with low surface charge, while CDI primarily removes charged species through electrostatic adsorption, resulting in suboptimal electrosorption efficiency for neutral/weakly charged organics. Furthermore, irreversible adsorption or redox reactions of organic compounds on electrode surfaces may cause fouling, compromising regeneration efficiency and operational lifespan. A novel approach involves pre-converting organic compounds into ionic species via auxiliary

technologies prior to CDI capture. Consequently, hybrid systems integrating CDI with electrochemical oxidation (EO), photocatalysis, and advanced oxidation processes (AOPs) have emerged as promising technological innovations. Wang et al. [174] coupled photocatalysis with CDI, wherein tetracycline (TC) is first adsorbed onto electrodes by the CDI component and subsequently decomposed via H^+ and ·OH radicals generated photocatalytically. This approach simultaneously achieves organic contaminant removal and mitigates organic-induced electrode fouling. In an innovative configuration, Lim et al. [175] integrated photoelectrochemical (PEC) oxidation with FCDI to establish a dual-function PEC-FCDI system. During brackish water treatment, this system produces highlyROS capable of degrading eight types of organic pollutants. Additionally, other studies have demonstrated the coupling of EO with CDI for the removal of sulfamethazine and sulfate ions [176].

Enhanced research on organic matter removal not only facilitates the advancement of desalination technologies toward real seawater applications but also promotes their market expansion into high-value sectors such as electronics, rare earth elements, and food processing. Although significant challenges persist in applying CDI for organic contaminant removal, concerted efforts are underway within this field. Looking forward, the integration of CDI systems with complementary technologies is anticipated, aiming to maximize synergistic effects.

6. Regulation

Electrode characteristics and operational parameters (e.g., voltage, current density, feed flow rate, salt concentration) critically govern CDI performance. Strategic optimization of these variables enables concurrent enhancement of desalination efficiency and reduction of energy consumption. Intelligent parameter regulation-achieving real-time water quality monitoring and dynamic operational adjustments through feedback mechanisms-constitutes a defining feature of modern CDI systems.

Prerequisite to intelligent control is elucidating the impact of individual CDI components on desalination capacity and energy expenditure. Of note is that in the practical application of FCDI, the system's energy consumption primarily originates from the resistance of the flow electrodes, the ion transport barriers across the IEMs, and the solution resistance within the desalination chamber. Among these, the energy consumption attributed to the flow electrodes is dominant under most operating conditions. Mitigating this electrode-related energy loss can be achieved through the optimization of flow electrode composition, the design of high-efficiency current collectors, and system-level architectural improvements [56]. Furthermore, operational parameters significantly influence energy consumption: while increasing the current density enhances the salt removal rate, it leads to a non-linear increase in energy demand and exacerbates concentration polarization. Raising the flow rate of the feed stream in the desalination chamber can reduce the transport resistance across IEMs to some extent, albeit at the cost of lower charge efficiency. Similarly, although increasing the flow rate of the flow electrode or its AC content improves electrode conductivity and reduces its specific energy consumption, it concurrently elevates the risk of clogging due to increased slurry viscosity and offers limited benefit for reducing energy consumption in the IEMs and desalination chamber [58,177,178]. Consequently, the development of steady-state process models or the implementation of model-based intelligent control strategies becomes a vital tool for deconvoluting the energy contributions of individual components, predicting system performance, and guiding the design and operational optimization of FCDI systems. Ultimately, achieving an optimal trade-off between energy efficiency and desalination performance is of paramount importance for advancing the practical implementation of FCDI technology. Wu et al. [179] employed a dynamic transport model with uncertainty quantification (UQ) to delineate the effects of electrode properties, operational conditions, and salt characteristics: (i) Pore size distribution and electrode connectivity critically modulate the effective diffusion coefficient, with macroporosity exerting predominant influence; (ii) Constant voltage (CV) operation is recommended for low-salinity wastewater to minimize resistive losses, whereas constant current (CC) mode proves optimal for high-salinity feeds. Zhu et al. [56] developed a steady-state FCDI model to quantify energy consumption distribution across components. By measuring potential drops and resistive losses in flow electrodes, IEMs, and desalination chambers, they established correlations between current density, desalination chamber flow rate, flow electrode velocity, and AC content. Their findings indicate flow electrodes dominate energy consumption in most scenarios. Parameter adjustments not only alter total energy usage but also reconfigure energy allocation among components.

ML enables computer systems to autonomously acquire knowledge from data and algorithms, thereby enhancing task performance. Pan et al. [180] employed ML methodologies to systematically investigate the structure-performance relationships among electrode materials, operational conditions, and CDI outcomes. By inputting characteristic parameters-including electrode dimensions, electrolyte concentration, applied voltage, and flow rate-into four ML models (Gradient Boosting (GB), Random Forest (RF), Support Vector Machine (SVM), and Artificial Neural Network (ANN)), they quantitatively evaluated predictive capabilities for desalination

metrics (SAC, ASAR). The GB model demonstrated statistically superior performance, achieving the lowest root mean square error (RMSE) for both SAC and ASAR predictions. SHapley Additive exPlanations (SHAP) analysis identified electrolyte concentration and SSA as the most critical determinants of desalination efficiency. This work establishes a robust correlation framework linking electrode properties, operational parameters, and desalination performance through ML-CDl integration, advancing intelligent CDI technology development.

Subsequent investigations have employed ANN [181], deep reinforcement learning (DRL) [182], and extended Fourier amplitude sensitivity testing (eFAST) [183] (Figure 12a–c) to predict CDI desalination capacity. Crucially, both ANN and eFAST analyses converge in identifying feed salinity concentration and current density as the dominant determinants of desalination performance. Consequently, moderate pretreatment of brackish water coupled with optimized current density selection is imperative for achieving high-efficiency desalination and maximized energy efficiency. Furthermore, DRL studies establish the soft actor-critic model as the optimal control strategy.

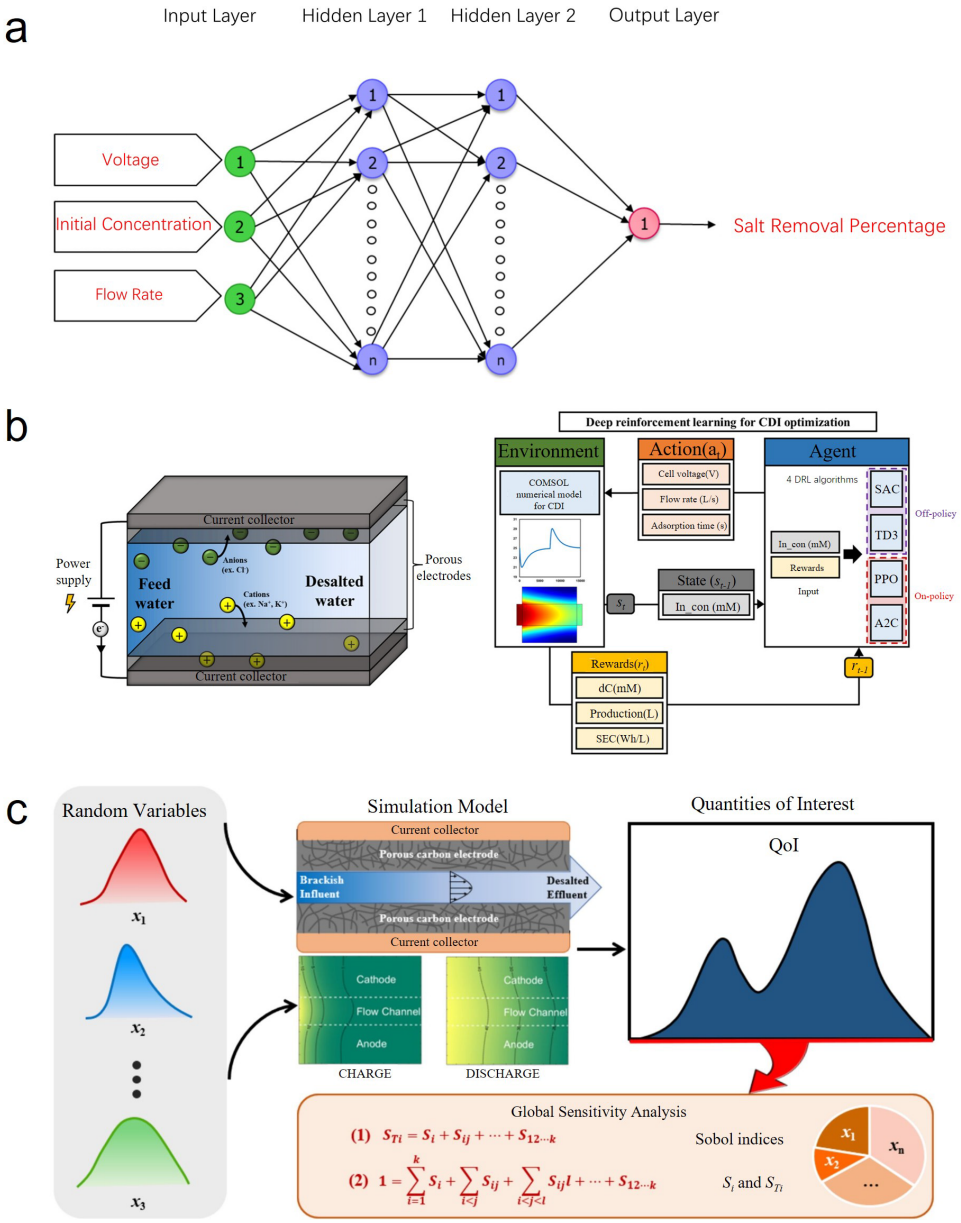

Figure 12. (**a**) Schematic of ANN structure with three layers of input, hidden (2 layer) and output along with input and output variables. Reprinted with permission from Ref. [181]. Copyright 2022, Elsevier. (**b**) Overall DRL structure for CDI optimization. In_con: influent salt concentration; dC: amount of removed salt; SEC: specific energy consumption; SAC: soft actor-critic; TD3: twin delayed deep deterministic policy gradients; PPO: proximal policy optimization; A2C: advantage actor-critic. Agents observe the state (s_{t-1}) and update the actions (a_t) to obtain the highest expected reward (r_t). Reprinted with permission from Ref. [182]. Copyright 2025, Elsevier. (**c**) Flow chart in implementation of the eFAST sensitivity analysis. Reprinted with permission from Ref. [183]. Copyright 2025, Elsevier.

The intelligent parameter regulation model utilizes sensors to monitor electrolyte concentration and ion species in real-time, coupled with ML models for dynamic adjustment of operational parameters such as applied voltage and flow rate. It automatically increases the applied voltage to enhance the adsorption driving force under high electrolyte concentration conditions, while lowering the voltage to reduce energy consumption during low electrolyte concentration periods. Furthermore, based on real-time predictions of electrode adsorption status (e.g., SAC), the system intelligently switches between adsorption and regeneration phases, minimizing efficiency loss due to electrode saturation. Additionally, the model predicts optimal electrodes and operational parameters for specific water sources in diverse application scenarios, thereby formulating rational operational strategies for CDI systems.

7. Summary and Future Perspectives

As an emerging desalination technology, CDI enables development of diverse standalone units and hybrid systems through continuous modifications to active electrode materials, device designs, and system architectures. Characterized by high energy efficiency, operational simplicity, low maintenance costs, environmental compatibility, and zero secondary pollution, CDI demonstrates substantial potential for desalinating low-to-moderate salinity brackish water.

Nevertheless, commercialization faces significant challenges: electrode material costs and lifespan remain critical constraints, where scalable manufacturing encounters high raw material expenses and complex synthesis processes-exemplified by CNTs and MXenes exhibiting superior performance yet prohibitive production costs. Prolonged operation induces electrode fouling and regeneration issues that degrade efficiency while increasing maintenance expenditures. Current CDI configurations exhibit limited treatment capacity, restricting applications to small-scale or low-salinity scenarios; scaling requires optimized flow channel designs and enhanced system integration. Balancing treatment efficiency and energy consumption proves particularly challenging for high-salinity feeds, where elevated voltages may trigger parasitic reactions compromising safety and cost-effectiveness. Furthermore, market adoption remains constrained by dominant conventional water treatment technologies, necessitating demonstrated superiority in reliability and economic viability for CDI to gain traction.

The HCDI system enhances conventional CDI desalination via faradaic reactions, with electrode materials being performance-determining. Transition metal oxides, MXene, and PBAs share structural advantages including open porous/layered architectures (providing abundant ion adsorption sites) and stable frameworks (ensuring long-term cycling stability). However, inherent limitations persist: poor conductivity of transition metal oxides necessitates conductive additives, while long-term cycling causes particle agglomeration and active site loss, leading to capacitance decay; despite high conductivity and surface area, MXene faces prohibitive synthesis costs and complex processing hindering industrial-scale implementation; PBAs risk metal ion leaching (potential environmental contamination) and undergo significant volume changes during ion insertion/extraction, causing structural collapse. Thus, continued material modification research must emphasize energy efficiency, cost reduction, and environmental sustainability-particularly through waste valorization. Advancing anode materials remains crucial for comprehensive HCDI system improvement.

In FCDI systems, optimizing conductive networks and adsorption/desorption performance is paramount due to the unique flowing electrode properties. Carbon material selection (AC/CB/CNTs), particle size distribution, and hybridization strategies significantly impact system performance and energy consumption. Beyond conventional carbons, eco-friendly biomass-derived alternatives show promise, with RM integration offering additional performance enhancement. Notably, Wu et al.'s innovative magnetic FCDI design addresses hydrodynamic challenges via flow path and velocity optimization. Current collectors play vital roles, where 3D collectors with hierarchical pore networks facilitate ion diffusion while reducing interfacial contact resistance through continuous conductive pathways. Their 3D structure homogenizes current distribution, mitigates side reactions from local overpotential, and improves energy utilization efficiency. Current collector optimization will remain a key research focus.

CDI demonstrates emerging potential for heavy metal and organic contaminant removal, though its practical efficacy requires comprehensive evaluation integrating pollutant properties, electrode materials, and environmental factors. Key advantages include voltage-or surface charge-mediated selective removal of heavy metals, mild operating conditions, low energy consumption, and compatibility with complementary technologies. However, significant challenges persist: complex pollutant compositions constrain adsorption mechanisms, high ionic strength reduces target contaminant adsorption capacity, while nonpolar/macromolecular organics cause pore blocking that impedes mass transfer-particularly rendering organic removal a critical bottleneck.

Current research disproportionately focuses on material development while neglecting system-level design considerations, constituting a fundamental barrier to commercialization. Future investigations should extend beyond

inorganic ion separation to encompass organic molecules and neutral substances. Strategic integration with advanced technologies could expand CDI applications from conventional groundwater/municipal wastewater treatment to high-value sectors like electronics, rare-earth processing, and food industries. Notably, many studies employ oversimplified conditions (e.g., single-component electrolytes simulating real water), ignoring real-world complexities such as trace ions, organic pollutants, and impurities that cause electrode fouling, side reactions, and energy loss. Theoretical models frequently oversimplify material-environment interactions, limiting practical relevance; performance metrics prioritize adsorption capacity while overlooking removal kinetics and energy efficiency.

As an energy-efficient separation technology, CDI necessitates not only continuous material optimization but also enhanced integration with complementary systems. Future designs should transcend singular component improvement and incorporate artificial intelligence for predictive model optimization, thereby enhancing operational precision and responsiveness to accelerate technological adoption. Figure 13 depicts the anticipated development of CDI. In the future, CDI is expected to achieve greater societal acceptance and find widespread application.

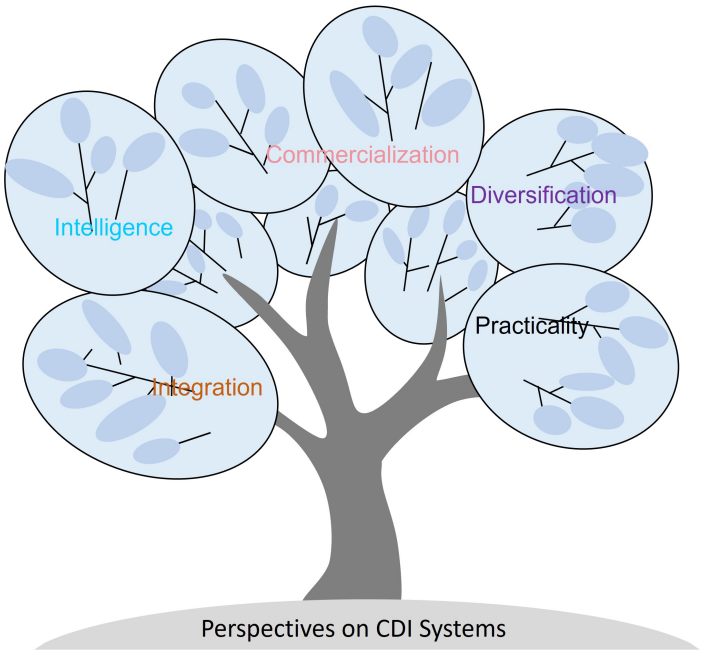

Figure 13. Summary of the future outlook for CDI.

Author Contributions

Y.G.: writing—original draft preparation, data curation, visualization; C.Y.: data curation, writing—reviewing and editing; R.W.: visualization, methodology; W.L.: conceptualization, supervision, writing—reviewing and editing, funding acquisition; H.P.: conceptualization, supervision, writing—reviewing and editing, funding acquisition. All authors have read and agreed to the published version of the manuscript.

Funding

This work was supported by the National Natural Science Foundation of China (NSFC-52371240, 22305212).

Institutional Review Board Statement

Not applicable.

Informed Consent Statement

Not applicable.

Data Availability Statement

Data will be made available on request.

Conflicts of Interest

The authors declare no conflict of interest. Given the role as Editor in Chief, Huan Pang had no involvement in the peer review of this paper and had no access to information regarding its peer-review process. Full responsibility for the editorial process of this paper was delegated to another editor of the journal.

Use of AI and AI-Assisted Technologies

No AI tools were utilized for this paper.

References

1. Shahid, M.U.; Najam, T.; Islam, M.; et al. Engineering of metal organic framework (MOF) membrane for waste water treatment: Synthesis, applications and future challenges. *J. Water Process Eng.* **2024**, *57*, 104676. https://doi.org/10.1016/j.jwpe.2023.104676.
2. Sun, K.; Tebyetekerwa, M.; Wang, C.; et al. Electrocapacitive Deionization: Mechanisms, Electrodes, and Cell Designs. *Adv. Funct. Mater.* **2023**, *33*, 2213578. https://doi.org/10.1002/adfm.202213578.
3. Musie, W.; Gonfa, G. Fresh water resource, scarcity, water salinity challenges and possible remedies: A review. *Heliyon* **2023**, *9*, e18685. https://doi.org/10.1016/j.heliyon.2023.e18685.
4. Chen, Z.; Ding, Z.; Chen, Y.; et al. Three-dimensional charge transfer pathway in close-packed nickel hexacyanoferrate−on−MXene nano-stacking for high-performance capacitive deionization. *Chem. Eng. J.* **2023**, *452*, 139451. https://doi.org/10.1016/j.cej.2022.139451.
5. Meng, F.; Ding, Z.; Xu, X.; et al. Metal organic framework-derived nitrogen-doped porous carbon sustained Prussian blue analogues for efficient and fast hybrid capacitive deionization. *Sep. Purif. Technol.* **2023**, *317*, 123899. https://doi.org/10.1016/j.seppur.2023.123899.
6. Wang, K.; Liu, Y.; Ding, Z.; et al. Chloride pre-intercalated CoFe-layered double hydroxide as chloride ion capturing electrode for capacitive deionization. *Chem. Eng. J.* **2022**, *433*, 133578. https://doi.org/10.1016/j.cej.2021.133578.
7. Cao, S.; Feng, W.; Tang, Y.; et al. Fabrication of CoTi-ZIF-9-derived carbon/MXene heterostructures for enhanced capacitive deionization in simulated seawater desalination. *Desalination* **2025**, *613*, 119059. https://doi.org/10.1016/j.desal.2025.119059.
8. Cao, S.; Li, Y.; Tang, Y.; et al. Space-Confined Metal Ion Strategy for Carbon Materials Derived from Cobalt Benzimidazole Frameworks with High Desalination Performance in Simulated Seawater. *Adv. Mater.* **2023**, *35*, 2301011. https://doi.org/10.1002/adma.202301011.
9. Liu, H.; Chen, B.; Chen, Y.; et al. Bioinspired Self-Standing, Self-Floating 3D Solar Evaporators Breaking the Trade-Off between Salt Cycle and Heat Localization for Continuous Seawater Desalination. *Adv. Mater.* **2023**, *35*, 2301596. https://doi.org/10.1002/adma.202301596.
10. Tang, Y.; Cao, S.; Feng, W.; et al. Spatial confinement effect on hollow mesoporous carbon spheres/MOF-derived nanosheets superstructures for improved capacitive deionization performance. *Nano Res.* **2025**, *18*, 94907194. https://doi.org/10.26599/nr.2025.94907194.
11. Tang, Y.; Shi, Y.; Su, Y.; et al. Enhanced Capacitive Deionization of Hollow Mesoporous Carbon Spheres/MOFs Derived Nanocomposites by Interface-Coating and Space-Encapsulating Design. *Adv. Sci.* **2024**, *11*, 2403802. https://doi.org/10.1002/advs.202403802.
12. Wu, X.; Lu, Y.; Ren, X.; et al. Interfacial Solar Evaporation: From Fundamental Research to Applications. *Adv. Mater.* **2024**, *36*, 2313090. https://doi.org/10.1002/adma.202313090.
13. Lawal, D.U.; Antar, M.A.; Ismaila, K.G.; et al. Hybrid multi-stage flash (MSF) and membrane distillation (MD) desalination system for energy saving and brine minimization. *Desalination* **2023**, *548*, 116231. https://doi.org/10.1016/j.desal.2022.116231.
14. Fritzmann, C.; Löwenberg, J.; Wintgens, T.; et al. State-of-the-art of reverse osmosis desalination. *Desalination* **2007**, *216*, 1–76. https://doi.org/10.1016/j.desal.2006.12.009.
15. Lim, Y.J.; Goh, K.; Kurihara, M.; et al. Seawater desalination by reverse osmosis: Current development and future challenges in membrane fabrication—A review. *J. Membr. Sci.* **2021**, *629*, 119292. https://doi.org/10.1016/j.memsci.2021.119292.
16. Liu, C.; Wang, W.; Yang, B.; et al. Separation, anti-fouling, and chlorine resistance of the polyamide reverse osmosis membrane: From mechanisms to mitigation strategies. *Water Res.* **2021**, *195*, 116976. https://doi.org/10.1016/j.watres.2021.116976.
17. Li, J.; Peng, H.; Liu, K.; et al. Polyester Nanofiltration Membranes for Efficient Cations Separation. *Adv. Mater.* **2023**, *36*, 2309406. https://doi.org/10.1002/adma.202309406.
18. Luo, J.; Wan, Y. Mix-charged nanofiltration membrane: Engineering charge spatial distribution for highly selective separation. *Chem. Eng. J.* **2023**, *464*, 142689. https://doi.org/10.1016/j.cej.2023.142689.
19. Yadav, D.; Karki, S.; Ingole, P.G. Current advances and opportunities in the development of nanofiltration (NF) membranes in the area of wastewater treatment, water desalination, biotechnological and pharmaceutical applications. *J. Environ. Chem. Eng.* **2022**, *10*, 108109. https://doi.org/10.1016/j.jece.2022.108109.

20. Zhao, R.; Jin, P.; Zhu, J.; et al. Amino acid-based loose polyamide nanofiltration membrane with ultrahigh water permeance for efficient dye/salt separation. *J. Membr. Sci.* **2023**, *673*, 121477. https://doi.org/10.1016/j.memsci.2023.121477.
21. Arana Juve, J.-M.; Christensen, F.M.S.; Wang, Y.; et al. Electrodialysis for metal removal and recovery: A review. *Chem. Eng. J.* **2022**, *435*, 134857. https://doi.org/10.1016/j.cej.2022.134857.
22. Sedighi, M.; Behvand Usefi, M.M.; Ismail, A.F.; et al. Environmental sustainability and ions removal through electrodialysis desalination: Operating conditions and process parameters. *Desalination* **2023**, *549*, 116319. https://doi.org/10.1016/j.desal.2022.116319.
23. Kumar, S.; Aldaqqa, N.M.; Alhseinat, E.; et al. Electrode Materials for Desalination of Water via Capacitive Deionization. *Angew. Chem. Int. Ed.* **2023**, *62*, e202302180. https://doi.org/10.1002/anie.202302180.
24. Zhang, S.; Xu, X.; Liu, X.; et al. Heterointerface optimization in a covalent organic framework-on-MXene for high-performance capacitive deionization of oxygenated saline water. *Mater. Horiz.* **2022**, *9*, 1708–1716. https://doi.org/10.1039/d1mh01882e.
25. Zhang, Y.; Wu, J.; Zhang, S.; et al. MOF-on-MOF nanoarchitectures for selectively functionalized nitrogen-doped carbon-graphitic carbon/carbon nanotubes heterostructure with high capacitive deionization performance. *Nano Energy* **2022**, *97*, 107146. https://doi.org/10.1016/j.nanoen.2022.107146.
26. Zhao, J.; Wu, B.; Huang, X.; et al. Efficient and Durable Sodium, Chloride-doped Iron Oxide-Hydroxide Nanohybrid-Promoted Capacitive Deionization of Saline Water via Synergetic Pseudocapacitive Process. *Adv. Sci.* **2022**, *9*, 2201678. https://doi.org/10.1002/advs.202201678.
27. He, Z.; Miller, C.J.; Zhu, Y.; et al. Membrane capacitive deionization (MCDI): A flexible and tunable technology for customized water softening. *Water Res.* **2024**, *259*, 121871. https://doi.org/10.1016/j.watres.2024.121871.
28. Xiao, Q.; Ma, J.; Xu, L.; et al. Membrane capacitive deionization (MCDI) for selective ion separation and recovery: Fundamentals, challenges, and opportunities. *J. Membr. Sci.* **2024**, *699*, 122650. https://doi.org/10.1016/j.memsci.2024.122650.
29. Zhu, Y.; Miller, C.; Lian, B.; et al. Brackish groundwater desalination by constant current membrane capacitive deionization (MCDI): Results of a long-term field trial in Central Australia. *Water Res.* **2024**, *254*, 121413. https://doi.org/10.1016/j.watres.2024.121413.
30. Jeon, S.-I.; Park, H.-R.; Yeo, J.-G.; et al. Desalination via a new membrane capacitive deionization process utilizing flow-electrodes. *Energy Environ. Sci.* **2013**, *6*, 1471. https://doi.org/10.1039/c3ee24443a.
31. Yang, F.; He, Y.; Rosentsvit, L.; et al. Flow-electrode capacitive deionization: A review and new perspectives. *Water Res.* **2021**, *200*, 117222. https://doi.org/10.1016/j.watres.2021.117222.
32. Zhang, C.; Ma, J.; Wu, L.; et al. Flow Electrode Capacitive Deionization (FCDI): Recent Developments, Environmental Applications, and Future Perspectives. *Environ. Sci. Technol.* **2021**, *55*, 4243–4267. https://doi.org/10.1021/acs.est.0c06552.
33. Gao, M.; Yang, Z.; Liang, W.; et al. Recent advanced freestanding pseudocapacitive electrodes for efficient capacitive deionization. *Sep. Purif. Technol.* **2023**, *324*, 124577. https://doi.org/10.1016/j.seppur.2023.124577.
34. Wei, B.; Liu, Z. Pseudo-capacitive behaviors induced dual-ion selective deionization system based on MoS2/PPy//Ag@PANI/AC. *Sep. Purif. Technol.* **2025**, *362*, 131906. https://doi.org/10.1016/j.seppur.2025.131906.
35. Zhou, X.; Shu, S.; Ye, X.; et al. Engineering Faradaic Electrode Materials for High-Efficiency Water Desalination. *Small* **2024**, *20*, 2400047. https://doi.org/10.1002/smll.202400047.
36. Liu, Y.; Gao, X.; Wang, Z.; et al. Controlled synthesis of bismuth oxychloride-carbon nanofiber hybrid materials as highly efficient electrodes for rocking-chair capacitive deionization. *Chem. Eng. J.* **2021**, *403*, 126326. https://doi.org/10.1016/j.cej.2020.126326.
37. Tu, X.; Liu, Y.; Wang, K.; et al. Ternary-metal Prussian blue analogues as high-quality sodium ion capturing electrodes for rocking-chair capacitive deionization. *J. Colloid Interface Sci.* **2023**, *642*, 680–690. https://doi.org/10.1016/j.jcis.2023.04.007.
38. Wang, H.; Liu, Y.; Li, Y.; et al. Tailoring the electrode material and structure of rocking-chair capacitive deionization for high-performance desalination. *Mater. Horiz.* **2024**, *11*, 5209–5219. https://doi.org/10.1039/d4mh00773e.
39. Liu, R.; Zhang, Q.; Shen, Y.; et al. Optimization of flow field distribution to improve desalination performance of battery electrode deionization by designing flow channel structure. *Sep. Purif. Technol.* **2024**, *331*, 125661. https://doi.org/10.1016/j.seppur.2023.125661.
40. Wei, W.; Feng, X.; Wang, R.; et al. Electrochemical Driven Phase Segregation Enabled Dual-Ion Removal Battery Deionization Electrode. *Nano Lett.* **2021**, *21*, 4830–4837. https://doi.org/10.1021/acs.nanolett.1c01487.
41. Wei, W.; Gu, X.; Wang, R.; et al. Wood-Based Self-Supporting Nanoporous Three-Dimensional Electrode for High-Efficiency Battery Deionization. *Nano Lett.* **2022**, *22*, 7572–7578. https://doi.org/10.1021/acs.nanolett.2c02583.
42. Gao, L.; Dong, Q.; Hu, C.; et al. Surfactant-assisted self-assembly of flower-like ultrathin vanadium disulfide nanosheets for enhanced hybrid capacitive deionization. *J. Colloid Interface Sci.* **2022**, *627*, 1011–1020. https://doi.org/10.1016/j.jcis.2022.07.111.
43. Chen, Z.; Xu, X.; Wang, K.; et al. Hybrid of pyrazine based π-conjugated organic molecule and MXene for hybrid capacitive deionization. *Sep. Purif. Technol.* **2023**, *315*, 123628. https://doi.org/10.1016/j.seppur.2023.123628.

44. Gong, S.; Liu, H.; Zhao, F.; et al. Vertically Aligned Bismuthene Nanosheets on MXene for High-Performance Capacitive Deionization. *ACS Nano* **2023**, *17*, 4843–4853. https://doi.org/10.1021/acsnano.2c11430.
45. Lei, J.; Xiong, Y.; Yu, F.; et al. Flexible self-supporting CoFe-LDH/MXene film as a chloride ions storage electrode in capacitive deionization. *Chem. Eng. J.* **2022**, *437*, 135381. https://doi.org/10.1016/j.cej.2022.135381.
46. Guo, Y.; Chen, Z.; Jiang, D.; et al. Evolution of CuCoFe Prussian blue analogues with open nanoframe architectures for enhanced capacitive deionization. *Chem. Eng. J.* **2024**, *495*, 153714. https://doi.org/10.1016/j.cej.2024.153714.
47. Lei, Y.; Wang, S.; Zhao, L.; et al. Entropy Engineering Constrain Phase Transitions Enable Ultralong-life Prussian Blue Analogs Cathodes. *Adv. Sci.* **2024**, *11*, 2402340. https://doi.org/10.1002/advs.202402340.
48. Sun, T.; Jia, M.; Zhang, H.; et al. Particle size reduction of manganese-doped Prussian blue analogues enhanced hybrid capacitive deionization performance. *Desalination* **2025**, *606*, 118787. https://doi.org/10.1016/j.desal.2025.118787.
49. Tran, N.A.T.; Khoi, T.M.; Phuoc, N.M.; et al. A review of recent advances in electrode materials and applications for flow-electrode desalination systems. *Desalination* **2022**, *541*, 116037. https://doi.org/10.1016/j.desal.2022.116037.
50. Hatzell, K.B.; Hatzell, M.C.; Cook, K.M.; et al. Effect of Oxidation of Carbon Material on Suspension Electrodes for Flow Electrode Capacitive Deionization. *Environ. Sci. Technol.* **2015**, *49*, 2368–2377. https://doi.org/10.1021/es5055989.
51. Aldaqqa, N.M.; Kumar, S.; Martínez, J.I.; et al. Surface Engineered 2D-β-ketoenamine Covalent Organic Framework for Superior Dechlorination via Hybrid Capacitive Deionization. *Angew. Chem. Int. Ed.* **2025**, *64*, e202510345. https://doi.org/10.1002/anie.202510345.
52. Lee, J.; Kim, S.; Kim, C.; et al. Hybrid capacitive deionization to enhance the desalination performance of capacitive techniques. *Energy Environ. Sci.* **2014**, *7*, 3683–3689. https://doi.org/10.1039/c4ee02378a.
53. Li, X.; Fu, X.; Zhang, Y.; et al. Electrospun sodium titanate-MXene/carbon nanofibers as binder-free electrode for enhanced hybrid capacitive deionization. *Chem. Eng. J.* **2025**, *511*, 162040. https://doi.org/10.1016/j.cej.2025.162040.
54. Yao, S.; Wang, D.; Fu, W.; et al. Unveiling the role of Atomic-Level "Pump-Driven" effect in MoS2/MnO2 for facilitating directional charge transfer in hybrid capacitive deionization. *Chem. Eng. J.* **2024**, *490*, 151608. https://doi.org/10.1016/j.cej.2024.151608.
55. Shin, Y.-U.; Lim, J.; Boo, C.; et al. Improving the feasibility and applicability of flow-electrode capacitive deionization (FCDI): Review of process optimization and energy efficiency. *Desalination* **2021**, *502*, 114930. https://doi.org/10.1016/j.desal.2021.114930.
56. Shi, C.; Wang, H.; Li, A.; et al. Process model for flow-electrode capacitive deionization for energy consumption estimation and system optimization. *Water Res.* **2023**, *230*, 119517. https://doi.org/10.1016/j.watres.2022.119517.
57. Wang, H.; Shi, C.; Zhu, G.; et al. Two-Phase flow model-driven optimization of charge percolation in flow-electrode capacitive deionization. *Water Res.* **2025**, *276*, 123283. https://doi.org/10.1016/j.watres.2025.123283.
58. Wang, L.; Zhang, C.; He, C.; et al. Equivalent film-electrode model for flow-electrode capacitive deionization: Experimental validation and performance analysis. *Water Res.* **2020**, *181*, 115917. https://doi.org/10.1016/j.watres.2020.115917.
59. Chen, Z.; Zhang, X.; Tang, Q.; et al. Achieving enhanced structural stability and electrical conductivity of MnHCF through Ni doping and CNT composite for efficient hybrid capacitive deionization. *J. Mater. Sci. Technol.* **2026**, *257*, 233–246. https://doi.org/10.1016/j.jmst.2025.08.049.
60. Li, X.; Yang, J.; Zhang, F.; et al. Orbital-Level Electronic Modulation of MnO_2 via Interfacial Built-In Electric Fields: Breaking the Jahn–Teller Distortion Cycle for Ultra-Durable Hybrid Capacitive Deionization. *Small* **2025**, *21*, 2505300. https://doi.org/10.1002/smll.202505300.
61. Zhuang, Z.; Sun, L.; Tao, Y.; et al. Highly Efficient and Stable Capacitive Deionization Based on a Flower-Like Conjugated Polymer with Double Active-Sites. *Energy Environ. Mater.* **2024**, *8*, e12852. https://doi.org/10.1002/eem2.12852.
62. Wei, H.; Wang, T.; Hu, R.; et al. Sulfur Vacancies Enriched Copper Sulfide Nanotubes Boost Desalination Efficiency of Hybrid Capacitive Deionization. *Small* **2025**, *21*, 2411810. https://doi.org/10.1002/smll.202411810.
63. Rommerskirchen, A.; Linnartz, C.J.; Egidi, F.; et al. Flow-electrode capacitive deionization enables continuous and energy-efficient brine concentration. *Desalination* **2020**, *490*, 114453. https://doi.org/10.1016/j.desal.2020.114453.
64. Yang, S.; Choi, J.; Yeo, J.-G.; et al. Flow-Electrode Capacitive Deionization Using an Aqueous Electrolyte with a High Salt Concentration. *Environ. Sci. Technol.* **2016**, *50*, 5892–5899. https://doi.org/10.1021/acs.est.5b04640.
65. Liu, X.; Xu, X.; Xuan, X.; et al. Unlocking Enhanced Capacitive Deionization of $NaTi_2(PO_4)_3$/Carbon Materials by the Yolk–Shell Design. *J. Am. Chem. Soc.* **2023**, *145*, 9242–9253. https://doi.org/10.1021/jacs.3c01755.
66. Chen, Z.; Xu, X.; Liu, Y.; et al. Ultra-durable and highly-efficient hybrid capacitive deionization by MXene confined MoS2 heterostructure. *Desalination* **2022**, *528*, 115616. https://doi.org/10.1016/j.desal.2022.115616.
67. Du, J.; Xing, W.; Yu, J.; et al. Synergistic effect of intercalation and EDLC electrosorption of 2D/3D interconnected architectures to boost capacitive deionization for water desalination via MoSe2/mesoporous carbon hollow spheres. *Water Res.* **2023**, *235*, 119831. https://doi.org/10.1016/j.watres.2023.119831.
68. Buczek, S.; Barsoum, M.L.; Uzun, S.; et al. Rational Design of Titanium Carbide MXene Electrode Architectures for Hybrid Capacitive Deionization. *Energy Environ. Mater.* **2020**, *3*, 398–404. https://doi.org/10.1002/eem2.12110.

69. Shi, X.-Y.; Gao, M.-H.; Hu, W.-W.; et al. Largely enhanced adsorption performance and stability of MXene through in-situ depositing polypyrrole nanoparticles. *Sep. Purif. Technol.* **2022**, *287*, 120596. https://doi.org/10.1016/j.seppur.2022.120596.
70. Xi, W.; Zhang, Y.; Hu, J.; et al. In-situ growth of Ni, Co-Prussian blue nanocubes on molten salt etched lamellar $Ti_3C_2T_x$/Ni for enhanced hybrid capacitive deionization. *Chem. Eng. J.* **2024**, *499*, 155941. https://doi.org/10.1016/j.cej.2024.155941.
71. Alfahel, R.; Tong, Y.; Pasha, M.; et al. A lamellar chitosan-lignosulfonate/MXene nanocomposite as binder-free electrode for high-performance capacitive deionization. *Desalination* **2024**, *573*, 117187. https://doi.org/10.1016/j.desal.2023.117187.
72. Zhang, T.; Chang, L.; Xiao, X. Surface and Interface Regulation of MXenes: Methods and Properties. *Small Methods* **2023**, *7*, 2201530. https://doi.org/10.1002/smtd.202201530.
73. Jiang, M.; Li, M.; Cui, C.; et al. Molecular-Level Interfacial Chemistry Regulation of MXene Enables Energy Storage beyond Theoretical Limit. *ACS Nano* **2024**, *18*, 7532–7545. https://doi.org/10.1021/acsnano.3c12329.
74. Wang, Q.; Su, X.; Jia, Y.; et al. Regulation of Microstructure and Absorption Properties of MXene Materials: Theoretical and Experimental. *Adv. Sci.* **2025**, *12*, e09994. https://doi.org/10.1002/advs.202509994.
75. Kong, W.; Lu, X.; Tan, K.; et al. Controlling electrode-potential distribution to enable oxidation stability of MXene-based CDI desalination cells. *Water Res.* **2025**, *284*, 123948. https://doi.org/10.1016/j.watres.2025.123948.
76. Wang, Y.; Zhang, X.; Liang, S.; et al. Exploring MXene's role in capacitive deionization: Advances, challenges, and future directions. *Chem. Eng. J.* **2024**, *496*, 154130. https://doi.org/10.1016/j.cej.2024.154130.
77. Zhang, S.; Zhao, Y.; Guo, K.; et al. Preparation of fully coated PEDOT: PSS film on MXene for high reliability capacitive deionization. *Desalination* **2025**, *594*, 118306. https://doi.org/10.1016/j.desal.2024.118306.
78. Gao, M.; Xiao, W.; Miao, L.; et al. Prussian blue and its analogs: A robust platform for efficient capacitive deionization. *Desalination* **2024**, *574*, 117278. https://doi.org/10.1016/j.desal.2023.117278.
79. Singh, K.; Li, G.; Lee, J.; et al. Divalent Ion Selectivity in Capacitive Deionization with Vanadium Hexacyanoferrate: Experiments and Quantum-Chemical Computations. *Adv. Funct. Mater.* **2021**, *31*, 2105203. https://doi.org/10.1002/adfm.202105203.
80. Wang, S.; Li, Z.; Wang, G.; et al. Freestanding $Ti_3C_2T_x$ MXene/Prussian Blue Analogues Films with Superior Ion Uptake for Efficient Capacitive Deionization by a Dual Pseudocapacitance Effect. *ACS Nano* **2021**, *16*, 1239–1249. https://doi.org/10.1021/acsnano.1c09036.
81. Zhao, B.; Wang, Y.; Wang, Z.; et al. Rational design of Core-Shell heterostructured CoFe@NiFe Prussian blue analogues for efficient capacitive deionization. *Chem. Eng. J.* **2024**, *487*, 150437. https://doi.org/10.1016/j.cej.2024.150437.
82. Li, B.; Wang, Y.; Huang, S.; et al. Co-doped Ni-PBA anchored on optimized ZIF-67-derived Co/N-doped hollow carbon framework for high-performance hybrid capacitive deionization. *Sep. Purif. Technol.* **2025**, *358*, 130257. https://doi.org/10.1016/j.seppur.2024.130257.
83. Zhou, W.; Huang, T.; Zhao, Y.; et al. Ternary-metal Prussian blue analog hollow spheres/MXene electrode based on self-assembly enabling highly stable capacitive deionization. *Chem. Eng. J.* **2025**, *508*, 161124. https://doi.org/10.1016/j.cej.2025.161124.
84. Xing, W.; Luo, K.; Liang, J.; et al. Urchin-like core–shell tungsten oxide@carbon composite electrode for highly efficient and stable water desalination via hybrid capacitive deionization (HCDI). *Chem. Eng. J.* **2023**, *477*, 147268. https://doi.org/10.1016/j.cej.2023.147268.
85. Bu, X.; Zhang, Y.; Guo, H.; et al. Enhanced hybrid capacitive deionization performance by the mass balance of electrodes. *Desalination* **2023**, *567*, 116982. https://doi.org/10.1016/j.desal.2023.116982.
86. Tang, Y.; Ding, J.; Zhou, W.; et al. Design of Uniform Hollow Carbon Nanoarchitectures: Different Capacitive Deionization between the Hollow Shell Thickness and Cavity Size. *Adv. Sci.* **2023**, *10*, 2206960. https://doi.org/10.1002/advs.202206960.
87. Chang, J.; Li, Y.; Duan, F.; et al. Selective removal of chloride ions by bismuth electrode in capacitive deionization. *Sep. Purif. Technol.* **2020**, *240*, 116600. https://doi.org/10.1016/j.seppur.2020.116600.
88. Yoon, H.; Lee, J.; Kim, S.; et al. Hybrid capacitive deionization with Ag coated carbon composite electrode. *Desalination* **2017**, *422*, 42–48. https://doi.org/10.1016/j.desal.2017.08.010.
89. Zhang, H.; Zhang, W.; Shen, J.; et al. Ag-doped hollow ZIFs-derived nanoporous carbon for efficient hybrid capacitive deionization. *Desalination* **2020**, *473*, 114173. https://doi.org/10.1016/j.desal.2019.114173.
90. Zhang, Z.; Li, H. Promoting the uptake of chloride ions by ZnCo–Cl layered double hydroxide electrodes for enhanced capacitive deionization. *Environ. Sci. Nano* **2021**, *8*, 1886–1895. https://doi.org/10.1039/d1en00350j.
91. Xu, M.; Tan, Z.; Tian, Y.; et al. Binder-free Bi@MXene film with 3D sandwich structure for highly hybrid capacitive deionization. *Sep. Purif. Technol.* **2025**, *363*, 132263. https://doi.org/10.1016/j.seppur.2025.132263.
92. Kim, N.; Park, J.; Cho, Y.; et al. Comprehensive Electrochemical Impedance Spectroscopy Study of Flow-Electrode Capacitive Deionization Cells. *Environ. Sci. Technol.* **2023**, *57*, 8808–8817. https://doi.org/10.1021/acs.est.3c01619.
93. Ma, J.; Chen, L.; Yu, F. Environmental applications and perspectives of flow electrode capacitive deionization (FCDI). *Sep. Purif. Technol.* **2024**, *335*, 126095. https://doi.org/10.1016/j.seppur.2023.126095.

94. Tan, Z.; Song, W.; Mao, X.; et al. Efficient capacitive deionization with hierarchical porous carbon flow electrodes. *Desalination* **2024**, *591*, 118051. https://doi.org/10.1016/j.desal.2024.118051.
95. Folaranmi, G.; Tauk, M.; Bechelany, M.; et al. Investigation of fine activated carbon as a viable flow electrode in capacitive deionization. *Desalination* **2022**, *525*, 115500. https://doi.org/10.1016/j.desal.2021.115500.
96. Tauk, M.; Bechelany, M.; Lagerge, S.; et al. Influence of particle size distribution on carbon-based flowable electrode viscosity and desalination efficiency in flow electrode capacitive deionization. *Sep. Purif. Technol.* **2023**, *306*, 122666. https://doi.org/10.1016/j.seppur.2022.122666.
97. Zhang, W.; Xue, W.; Xiao, K.; et al. Selection and optimization of carbon-based electrode materials for flow-electrode capacitive deionization. *Sep. Purif. Technol.* **2023**, *315*, 123649. https://doi.org/10.1016/j.seppur.2023.123649.
98. Han, M.; Tang, L.; Xiao, Y.; et al. Enhanced continuous desalination performance with iron-complexed malonate redox couples. *Environ. Sci. Water Res. Technol.* **2023**, *9*, 2368–2377. https://doi.org/10.1039/d3ew00400g.
99. Qi, F.; Wang, X.; Zhu, P.; et al. Asymmetric Fe^{2+}/Fe^{3+}-Mediated Flow-Electrode Capacitive Deionization for the Removal of Chloride Ions in Reclaimed Water. *ACS Sustain. Chem. Eng.* **2024**, *12*, 8609–8619. https://doi.org/10.1021/acssuschemeng.4c00071.
100. Lwin, T.T.A.; Chen, X.; Zaw, M.; et al. Enhanced desalination performance of flow capacitive deionization with the addition of conductive polymer in redox couples and activated carbon. *Carbon* **2025**, *231*, 119703. https://doi.org/10.1016/j.carbon.2024.119703.
101. Wei, Q.; Hu, Y.; Wang, J.; et al. Low energy consumption flow capacitive deionization with a combination of redox couples and carbon slurry. *Carbon* **2020**, *170*, 487–492. https://doi.org/10.1016/j.carbon.2020.07.044.
102. Wei, Q.; Tang, L.; Ramalingam, K.; et al. Redox-catalysis flow electrode desalination in an organic solvent. *J. Mater. Chem. A* **2021**, *9*, 22254–22261. https://doi.org/10.1039/d1ta05350g.
103. Luo, L.; He, Q.; Yi, D.; et al. Indirect charging of carbon by aqueous redox mediators contributes to the enhanced desalination performance in flow-electrode CDI. *Water Res.* **2022**, *220*, 118688. https://doi.org/10.1016/j.watres.2022.118688.
104. Mani, S.; Thangapandi, B.; Elangovan, P.; et al. New insights into the performance analysis of flow-electrode capacitive deionization using ferri/ferrocyanide redox couples for continuous water desalination. *Chem. Eng. J.* **2024**, *480*, 147887. https://doi.org/10.1016/j.cej.2023.147887.
105. Freire, N.H.J.; Linnartz, C.J.; Montoro, L.A.; et al. Flow electrode capacitive deionization with iron-based redox electrolyte. *Desalination* **2024**, *578*, 117313. https://doi.org/10.1016/j.desal.2024.117313.
106. Alawad, S.M.; Mansour, R.B.; Al-Sulaiman, F.A.; et al. Renewable energy systems for water desalination applications: A comprehensive review. *Energy Convers. Manag.* **2023**, *286*, 117035. https://doi.org/10.1016/j.enconman.2023.117035.
107. Luo, K.; Chen, M.; Xing, W.; et al. Significantly enhanced desalination performance of flow-electrode capacitive deionization via cathodic iodide redox couple and its great potential in treatment of iodide-containing saline wastewater. *Chem. Eng. J.* **2021**, *421*, 129905. https://doi.org/10.1016/j.cej.2021.129905.
108. Wei, Q.; Cui, C.; Wang, Z.; et al. Enhanced phosphate removal and recovery from wastewater by flow-electrode capacitive deionization (FCDI): Role of $[Fe(CN)6]^{3-/4-}$ redox couple. *Water Res.* **2025**, *277*, 123304. https://doi.org/10.1016/j.watres.2025.123304.
109. Wu, L.; Garg, S.; Waite, T.D. Progress and challenges in the use of electrochemical oxidation and reduction processes for heavy metals removal and recovery from wastewaters. *J. Hazard. Mater.* **2024**, *479*, 135581. https://doi.org/10.1016/j.jhazmat.2024.135581.
110. Yang, J.; Peng, J.; Zhang, P.; et al. A redox-mediated polymer with extended π-delocalization for efficient Cr^{3+} elimination via capacitive deionization. *Sep. Purif. Technol.* **2025**, *368*, 133039. https://doi.org/10.1016/j.seppur.2025.133039.
111. Xiong, L.; Tang, J. Strategies and Challenges on Selectivity of Photocatalytic Oxidation of Organic Substances. *Adv. Energy Mater.* **2021**, *11*, 2003216. https://doi.org/10.1002/aenm.202003216.
112. Chen, R.; Deng, X.; Wang, C.; et al. Enhanced desalination performances by using porous polyaniline-activated carbon composite flow-electrodes in capacitive deionization system. *Desalination* **2023**, *557*, 116568. https://doi.org/10.1016/j.desal.2023.116568.
113. Chen, K.-Y.; Shen, Y.-Y.; Wang, D.-M.; et al. Carbon nanotubes/activated carbon hybrid as a high-performance suspension electrode for the electrochemical desalination of wastewater. *Desalination* **2022**, *522*, 115440. https://doi.org/10.1016/j.desal.2021.115440.
114. Minh Phuoc, N.; Anh Thu Tran, N.; Minh Khoi, T.; et al. ZIF-67 metal-organic frameworks and CNTs-derived nanoporous carbon structures as novel electrodes for flow-electrode capacitive deionization. *Sep. Purif. Technol.* **2021**, *277*, 119466. https://doi.org/10.1016/j.seppur.2021.119466.
115. Rauer, S.B.; Wang, S.; Köller, N.; et al. PEDOT:PSS-CNT Composite Particles Overcome Contact Resistances in Slurry Electrodes for Flow-Electrode Capacitive Deionization. *Adv. Funct. Mater.* **2023**, *33*, 2303606. https://doi.org/10.1002/adfm.202303606.

116. Yan, L.; Issaka Alhassan, S.; Gang, H.; et al. Enhancing charge transfer utilizing ternary composite slurry for high-efficient flow-electrode capacitive deionization. *Chem. Eng. J.* **2023**, *468*, 143413. https://doi.org/10.1016/j.cej.2023.143413.
117. Cai, Y.; Zhao, F.; Zhao, J.; et al. Flexible construction of three-dimensional continuous conductive structure by hollow carbon sphere and CNT for promoted ions transport in flow-electrode capacitive deionization. *Sep. Purif. Technol.* **2024**, *337*, 126405. https://doi.org/10.1016/j.seppur.2024.126405.
118. Alsultan, A.; Alkhaldi, A.; Alsaikhan, K.; et al. Surface-treated carbon black for durable, efficient, continuous flow electrode capacitive deionization. *Sep. Purif. Technol.* **2023**, *313*, 123444. https://doi.org/10.1016/j.seppur.2023.123444.
119. Wang, C.; Wu, X.; Wang, F.; et al. Pine-derived porous carbon for efficient capacitive deionization and the role of its hierarchical pore structure. *Sep. Purif. Technol.* **2024**, *342*, 126865. https://doi.org/10.1016/j.seppur.2024.126865.
120. Yang, R.; Xu, X.; Teng, J.; et al. Porous carbon flow-electrode derived from modified MOF-5 for capacitive deionization. *Desalination* **2024**, *569*, 117077. https://doi.org/10.1016/j.desal.2023.117077.
121. Xu, Y.; Duan, F.; Cao, R.; et al. Enhanced salt removal performance using nickel hexacyanoferrate/carbon nanotubes as flow cathode in asymmetric flow electrode capacitive deionization. *Desalination* **2023**, *566*, 116929. https://doi.org/10.1016/j.desal.2023.116929.
122. Xu, L.; Peng, S.; Mao, Y.; et al. Enhancing Brackish Water Desalination using Magnetic Flow-electrode Capacitive Deionization. *Water Res.* **2022**, *216*, 118290. https://doi.org/10.1016/j.watres.2022.118290.
123. Xu, L.; Tang, L.; Peng, S.; et al. Magnetic array for efficient and stable Flow-electrode capacitive deionization. *Chem. Eng. J.* **2022**, *446*, 137415. https://doi.org/10.1016/j.cej.2022.137415.
124. Xu, L.; Peng, S.; Wu, K.; et al. Precise manipulation of the charge percolation networks of flow-electrode capacitive deionization using a pulsed magnetic field. *Water Res.* **2022**, *222*, 118963. https://doi.org/10.1016/j.watres.2022.118963.
125. Chen, R.; Deng, X.; Wang, C.; et al. A newly designed graphite-polyaniline composite current collector to enhance the performance of flow electrode capacitive deionization. *Chem. Eng. J.* **2022**, *435*, 134845. https://doi.org/10.1016/j.cej.2022.134845.
126. Zhang, X.; Zhou, H.; He, Z.; et al. Flow-electrode capacitive deionization utilizing three-dimensional foam current collector for real seawater desalination. *Water Res.* **2022**, *220*, 118642. https://doi.org/10.1016/j.watres.2022.118642.
127. Zhang, X.; Pang, M.; Wei, Y.; et al. Three-dimensional titanium mesh-based flow electrode capacitive deionization for salt separation and enrichment in high salinity water. *Water Res.* **2024**, *251*, 121147. https://doi.org/10.1016/j.watres.2024.121147.
128. Zhai, C.; Yuan, J.; Wang, Y.; et al. Rectorite in flow-electrode capacitive deionization with three-dimensional current collector to achieve cost-effective desalination. *Desalination* **2024**, *573*, 117217. https://doi.org/10.1016/j.desal.2023.117217.
129. Zhang, X.; Zhou, J.; Zhou, H.; et al. Enhanced Desalination Performance by a Novel Archimedes Spiral Flow Channel for Flow-Electrode Capacitive Deionization. *ACS EST Eng.* **2022**, *2*, 1250–1259. https://doi.org/10.1021/acsestengg.1c00445.
130. He, X.; Chen, W.; Sun, F.; et al. Enhanced NH^{4+} Removal and Recovery from Wastewater Using Na-Zeolite-based Flow-Electrode Capacitive Deionization: Insight from Ion Transport Flux. *Environ. Sci. Technol.* **2023**, *57*, 8828–8838. https://doi.org/10.1021/acs.est.3c02286.
131. Ma, J.; Wang, X.; Bian, Y.; et al. Novel Current Collector with Mosquito-Repellent Incense-Shaped Channel of Flow Electrode Capacitive Deionization. *ACS Sustain. Chem. Eng.* **2022**, *10*, 4818–4821. https://doi.org/10.1021/acssuschemeng.2c00442.
132. Yan, L.; Annor Asare, J.; Wu, B.; et al. A Hexagonal Honeycomb-Shaped Flow Channel for High-Efficient Desalination and Flowability in Flow-Electrode Capacitive Deionization. *ACS EST Water* **2023**, *3*, 2753–2764. https://doi.org/10.1021/acsestwater.3c00242.
133. Saif, H.M.; Gebregeorgis, T.H.; Crespo, J.G.; et al. The influence of flow electrode channel design on flow capacitive deionization performance: Experimental and CFD modelling insights. *Desalination* **2024**, *578*, 117452. https://doi.org/10.1016/j.desal.2024.117452.
134. Zhang, H.; Li, Y.; Han, J.; et al. Influence of ion exchange membrane arrangement on dual-channel flow electrode capacitive deionization: Theoretical analysis and experimentations. *Desalination* **2023**, *548*, 116288. https://doi.org/10.1016/j.desal.2022.116288.
135. Xie, B.; Liu, Q.; Tan, G.; et al. A novel four-chamber flow electrode capacitive deionization system for continuous recovery of heavy metal ions from wastewater. *Sep. Purif. Technol.* **2023**, *319*, 124055. https://doi.org/10.1016/j.seppur.2023.124055.
136. Liu, L.; Wu, J.; Wang, Z.; et al. A novel cell structure for high performance electrosorption process. *Desalination* **2025**, *601*, 118603. https://doi.org/10.1016/j.desal.2025.118603.
137. Chen, R.; Liu, X.; Wang, M.; et al. A novel two-stage continuous capacitive deionization system with connected flow electrode and freestanding electrode. *Chem. Eng. J.* **2024**, *491*, 152133. https://doi.org/10.1016/j.cej.2024.152133.
138. Hossain, S.M.; Yu, H.; Choo, Y.; et al. ZiF-8 induced carbon electrodes for selective lithium recovery from aqueous feed water by employing capacitive deionization system. *Desalination* **2023**, *546*, 116201. https://doi.org/10.1016/j.desal.2022.116201.
139. Si, J.; Xue, C.; Li, S.; et al. Selective membrane capacitive deionization for superior lithium recovery. *Desalination* **2024**, *572*, 117154. https://doi.org/10.1016/j.desal.2023.117154.

140. Hong, S.P.; Yoon, H.; Lee, J.; et al. Selective phosphate removal using layered double hydroxide/reduced graphene oxide (LDH/rGO) composite electrode in capacitive deionization. *J. Colloid Interface Sci.* **2020**, *564*, 1–7. https://doi.org/10.1016/j.jcis.2019.12.068.
141. Bao, Y.; Miao, S.; Yin, P.; et al. Optimization of NiHCF/MnO_2 composite electrodes for lithium extraction via capacitive deionization: A case of core-shell construction strategy. *Chem. Eng. J.* **2025**, *525*, 170471. https://doi.org/10.1016/j.cej.2025.170471.
142. Dhanushkotti, R.; Mohammed, A.K.; Ranjeesh, K.C.; et al. Inherited Nitrogen Distribution Control in Covalent Organic Framework Cathodes for Efficient Electrochemical Lithium Recovery via Capacitive Deionization. *Adv. Sci.* **2025**, *12*, 2417140. https://doi.org/10.1002/advs.202417140.
143. Ma, G.; Zhang, X.; Cai, A.; et al. Lithium extraction from salt lake brine by four-stage ion-distillation of flow electrode capacitive deionization. *Chem. Eng. J.* **2024**, *493*, 152519. https://doi.org/10.1016/j.cej.2024.152519.
144. Bae, S.; Kim, Y.; Kim, S.; et al. Enhanced sulfate ion adsorption selectivity in capacitive deionization with ball-milled activated carbon. *Desalination* **2022**, *540*, 116014. https://doi.org/10.1016/j.desal.2022.116014.
145. Zhang, J.; Xu, B.; Wang, Z.; et al. Efficient phosphorus removal from ultra-low concentration wastewater by flow-electrode capacitive deionization. *Sep. Purif. Technol.* **2024**, *341*, 126973. https://doi.org/10.1016/j.seppur.2024.126973.
146. Zhang, H.; Wang, Q.; Li, L.; et al. Electric double layer capacitive adsorption and faradaic pseudo-capacitance behavior of ZnFe-PANI/CNT electrode for phosphate removal in capacitive deionization. *Sep. Purif. Technol.* **2024**, *333*, 125913. https://doi.org/10.1016/j.seppur.2023.125913.
147. Wang, H.; You, H.; Wu, G.; et al. Co/Fe co-doped ZIF-8 derived hierarchically porous composites as high-performance electrode materials for Cu^{2+} ions capacitive deionization. *Chem. Eng. J.* **2023**, *460*, 141621. https://doi.org/10.1016/j.cej.2023.141621.
148. Wang, S.; Zhuang, H.; Shen, X.; et al. Copper removal and recovery from electroplating effluent with wide pH ranges through hybrid capacitive deionization using CuSe electrode. *J. Hazard. Mater.* **2023**, *457*, 131785. https://doi.org/10.1016/j.jhazmat.2023.131785.
149. Shen, X.; Wang, S.; Zhao, L.; et al. Simultaneous Cu(II)-EDTA decomplexation and Cu(II) recovery using integrated contact-electro-catalysis and capacitive deionization from electroplating wastewater. *J. Hazard. Mater.* **2024**, *472*, 134548. https://doi.org/10.1016/j.jhazmat.2024.134548.
150. Gao, Z.; Wang, L.; Huang, X.; et al. Selective single-atom adsorption for precision separation of lead ions in tap water via capacitive deionization. *Water Res.* **2025**, *268*, 122665. https://doi.org/10.1016/j.watres.2024.122665.
151. Wang, R.; Xu, B.; Chen, Y.; et al. Electro-enhanced adsorption of lead ions from slightly-polluted water by capacitive deionization. *Sep. Purif. Technol.* **2022**, *282*, 120122. https://doi.org/10.1016/j.seppur.2021.120122.
152. Datar, S.D.; Mane, R.S.; Kumar, N.; et al. Effective removal of heavy metal-lead and inorganic salts by microporous carbon derived from Zeolitic Imidazolate Framework-67 electrode using capacitive deionization. *Desalination* **2023**, *558*, 116619. https://doi.org/10.1016/j.desal.2023.116619.
153. Mao, M.; Yan, T.; Chen, G.; et al. Selective Capacitive Removal of Pb^{2+} from Wastewater over Redox-Active Electrodes. *Environ. Sci. Technol.* **2020**, *55*, 730–737. https://doi.org/10.1021/acs.est.0c06562.
154. Tang, C.; Li, Y.; Yu, Y.; et al. Selective capacitive removal of Pb(II) ions from industrial wastewater using NF/Mn_2CoO_4@MoO_2 electrodes. *Chem. Eng. J.* **2024**, *495*, 153196. https://doi.org/10.1016/j.cej.2024.153196.
155. Liu, D.; Xu, S.; Cai, Y.; et al. A coupling technology of capacitive deionization and carbon-supported petal-like VS_2 composite for effective and selective adsorption of lead (II) ions. *J. Electroanal. Chem.* **2022**, *910*, 116152. https://doi.org/10.1016/j.jelechem.2022.116152.
156. Gao, Y.; Xu, Y.; Xiang, S.; et al. Nitrogen-doped carbon nanotube encapsulated Fe_7S_8 nanoparticles for the high-efficiency and selective removal of Pb^{2+} by pseudocapacitive coupling. *Environ. Sci. Nano* **2022**, *9*, 2051–2060. https://doi.org/10.1039/d2en00044j.
157. Zhang, H.; Li, X.; Xiao, C.; et al. Enhanced selective electrosorption of Pb^{2+} from complex water on covalent organic framework-reduced graphene oxide nanocomposite. *Sep. Purif. Technol.* **2022**, *302*, 122147. https://doi.org/10.1016/j.seppur.2022.122147.
158. Wang, Y.; Chen, W.; Yang, X.; et al. Enhanced removal of lead ions from wastewaters by electrochemical adsorption using nitrogen-doped $Ti_3C_2T_x$ MXene. *Chem. Eng. J.* **2024**, *498*, 155463. https://doi.org/10.1016/j.cej.2024.155463.
159. Yang, D.; Li, X.; Li, Y.; et al. Capacitive deionization of high concentrations of hexavalent chromium using nickel–ferric-layered double hydroxide/molybdenum disulfide asymmetric electrode. *J. Colloid Interface Sci.* **2023**, *634*, 793–803. https://doi.org/10.1016/j.jcis.2022.12.100.
160. Nguyen, T.K.A.; Huynh, T.V.; Doong, R.-A. Enhanced capacitive deionization of Cr(VI) using functionalized metal carbide 2D framework and badam tree leaf-derived carbon as the asymmetric electrode materials. *Chem. Eng. J.* **2023**, *475*, 146439. https://doi.org/10.1016/j.cej.2023.146439.

161. Yang, D.; Wang, L.; Li, Y.; et al. Pseudocapacitive deionization of high concentrations of hexavalent chromium using NiFe-layered double hydroxide/polypyrrole asymmetric electrode. *Sep. Purif. Technol.* **2024**, *328*, 125004. https://doi.org/10.1016/j.seppur.2023.125004.
162. Zhang, X.; Wang, Z.; Guo, X. Confinement-induced Ni-based MOF formed on $Ti_3C_2T_x$ MXene support for enhanced capacitive deionization of chromium(VI). *Sci. Rep.* **2025**, *15*, 3727. https://doi.org/10.1038/s41598-025-87642-z.
163. Wu, P.-C.; Viet Cuong, D.; Wu, J.-C.; et al. Harnessing in-situ electrocatalytic oxidation with a cobalt oxide decorated nanocomposite electrode for efficient arsenic removal in capacitive deionization. *Chem. Eng. J.* **2023**, *474*, 145887. https://doi.org/10.1016/j.cej.2023.145887.
164. Cai, L.; Xu, B.; Gan, Y.; et al. Effective removal of trace arsenic from groundwater by capacitive deionization. *Sep. Purif. Technol.* **2024**, *330*, 125419. https://doi.org/10.1016/j.seppur.2023.125419.
165. Garzón-Pérez, A.; Vilasó-Cadre, J.; Balderas, P.; et al. Capacitive deionization with Mg/Al mixed oxides for arsenic removal from water. *J. Environ. Chem. Eng.* **2025**, *13*, 116578. https://doi.org/10.1016/j.jece.2025.116578.
166. Gong, W.; Yang, Y.; Chang, H.; et al. Evaluating the performance of flow-electrode capacitive deionization for cadmium removal from aqueous solution. *J. Water Process Eng.* **2022**, *46*, 102595. https://doi.org/10.1016/j.jwpe.2022.102595.
167. Mai, S.; Huang, H.; Long, J.; et al. Enhanced simultaneous removal of thallium and cadmium using flow-electrode capacitive deionization. *J. Environ. Chem. Eng.* **2025**, *13*, 116938. https://doi.org/10.1016/j.jece.2025.116938.
168. Zhou, J.; Zhang, X.; Zhang, Y.; et al. Effective inspissation of uranium(VI) from radioactive wastewater using flow electrode capacitive deionization. *Sep. Purif. Technol.* **2022**, *283*, 120172. https://doi.org/10.1016/j.seppur.2021.120172.
169. Wang, D.; Wang, J.; Zhang, D.; et al. Efficient remediation and synchronous recovery of uranium by phosphate-functionalized magnetic carbon-based flow electrode capacitive deionization. *Water Res.* **2025**, *281*, 123707. https://doi.org/10.1016/j.watres.2025.123707.
170. Wang, Z.; Kou, J.; Li, M.; et al. Enhancement and sustained uranium removal of 2D transition metal sulfide-graphene oxide composite/carbon cloth cathodes in capacitive deionization system. *Desalination* **2025**, *605*, 118745. https://doi.org/10.1016/j.desal.2025.118745.
171. Li, W.; Kang, W.; Ye, C.; et al. Zirconium-based MOF/MXene aerogel composite for highly stable and selective capture of uranium from aqueous solution. *Appl. Surf. Sci.* **2025**, *702*, 163323. https://doi.org/10.1016/j.apsusc.2025.163323.
172. Zhang, Z.; Li, J.; Meng, N.; et al. Simultaneously-efficient electro-sorption of Pb(II), Cu(II) and Cd(II) by Cu^{2+} modified superactive carbons. *Sep. Purif. Technol.* **2024**, *338*, 126604. https://doi.org/10.1016/j.seppur.2024.126604.
173. Zhang, B.; Yi, Q.; Qu, W.; et al. Titanium Carbon Oxide Flakes with Tunable Interlayer Spacing for Efficient Capacitive Deionization. *Adv. Funct. Mater.* **2024**, *34*, 2401332. https://doi.org/10.1002/adfm.202401332.
174. Li, Z.; Zhou, H.; Li, W.; et al. Cooperative reinforcement of photocatalysis-coupled capacitive deionization in fructose intercalated MoS_2 for removal of tetracycline. *Sep. Purif. Technol.* **2024**, *331*, 125583. https://doi.org/10.1016/j.seppur.2023.125583.
175. Lim, J.; Shin, Y.-U.; Son, A.; et al. TiO_2 nanotube electrode for organic degradation coupled with flow-electrode capacitive deionization for brackish water desalination. *NPJ Clean Water* **2022**, *5*, 7. https://doi.org/10.1038/s41545-022-00150-9.
176. Ge, Y.; Li, X.; Zheng, Z.; et al. Simultaneous removal of sulfamethazine and sulfate via electrochemical oxidation and capacitive Deionization: Mechanisms of in-situ activation and strategies of the hybrid system. *Sep. Purif. Technol.* **2024**, *344*, 127202. https://doi.org/10.1016/j.seppur.2024.127202.
177. Dahiya, S.; Mishra, B.K. Enhancing understandability and performance of flow electrode capacitive deionisation by optimizing configurational and operational parameters: A review on recent progress. *Sep. Purif. Technol.* **2020**, *240*, 116660. https://doi.org/10.1016/j.seppur.2020.116660.
178. Tang, K.; Yiacoumi, S.; Li, Y.; et al. Optimal conditions for efficient flow-electrode capacitive deionization. *Sep. Purif. Technol.* **2020**, *240*, 116626. https://doi.org/10.1016/j.seppur.2020.116626.
179. Mao, Y.; Long, S.; Kuai, X.; et al. Statistical uncertainty quantification to augment CDI electrode design and operation optimization. *Chem. Eng. J.* **2023**, *469*, 143825. https://doi.org/10.1016/j.cej.2023.143825.
180. Wang, H.; Jiang, M.; Xu, G.; et al. Machine Learning-Guided Prediction of Desalination Capacity and Rate of Porous Carbons for Capacitive Deionization. *Small* **2024**, *20*, 2401214. https://doi.org/10.1002/smll.202401214.
181. Salari, K.; Zarafshan, P.; Khashehchi, M.; et al. Modeling and predicting of water production by capacitive deionization method using artificial neural networks. *Desalination* **2022**, *540*, 115992. https://doi.org/10.1016/j.desal.2022.115992.
182. Lee, S.; Shim, J.; Kim, H.H.; et al. Optimizing capacitive deionization operation using dynamic modeling and reinforcement learning. *Desalination* **2025**, *602*, 118626. https://doi.org/10.1016/j.desal.2025.118626.
183. Qin, H.; Fang, F.; Mao, Y.; et al. Insights on CDI parametric controls and dependencies using gloabal sensitivity analysis. *Sep. Purif. Technol.* **2025**, *354*, 129424. https://doi.org/10.1016/j.seppur.2024.129424.